THE DESIGN AND QUALIFICATION OF THE UGA WATER TUNNEL

By

MICHAEL ADEMOLA OYEYEMI

(Under the Direction of Ben Davis)

ABSTRACT

The Dynamic Devices and Solutions Lab at the University of Georgia (UGA) recently installed a high-speed water tunnel to conduct fluid-structure interaction (FSI) experiments. The tunnel is custom-designed to deliver uniform flow up to 10 m/s through a square test section. This work presents an overview of water tunnels, their primary components, and their functions. It details the design and fabrication of key components of the UGA water tunnel and provides justification for design decisions. It discusses instruments for measuring velocity and turbulence and for flow visualization. The qualification procedure and results are also described. Tunnel flow parameters were identified using a laser doppler anemometry system, and results show that the water tunnel generates uniform, laminar flow within the test section for flow speeds between 1 and 10 m/s, while also maintaining boundary layer thicknesses below 35 mm. Turbulence intensity values averaged 0.50% for flow outside the boundary layer.

INDEX WORDS: high-speed, water tunnel, fluid-structure interaction, qualification, design, fabrication, laser doppler anemometry

THE DESIGN AND QUALIFICATION OF THE UGA WATER TUNNEL

By

MICHAEL ADEMOLA OYEYEMI

B.S., The University of Georgia, 2016

A Thesis Submitted to the Graduate Faculty of The University of Georgia in Partial Fulfillment of the Requirements for the Degree

MASTER OF SCIENCE

ATHENS, GEORGIA

2018

THE DESIGN AND QUALIFICATION OF THE UGA WATER TUNNEL

By

MICHAEL ADEMOLA OYEYEMI

Major Professor: Ben Davis

Committee: Thomas Lawrence
Brock Woodson

Electronic Version Approved:

Suzanne Barbour
Dean of the Graduate School
The University of Georgia
May 2018

Contents

Nomenclature

$\dot{m}$ Mass flow rate

ϕ_{half} Diffuser half angle

ρ_w Water density

A, B, C Antoine equation constants

a_C, b_C, c_C... Contraction polynomial shape coefficients

a_{in} Diffuser inlet length

a_{out} Diffuser outlet length

A_{ts} Test section cross-sectional area

Ca Cavitation number

h_{ts} Test section height

L_C Contraction cone length

L_D Diffuser length

l_{ts} Test section length

p_v Water vapor pressure

P_{fl} Motor power with fluid loss adjustment

p_{min} Mimimum pressure

P_{nl} Motor power without fluid loss adjustment

r_c Contraction ratio

r_e Energy ratio

T Temperature

Tr Toor to Pa conversion factor

U_c Velocity at test section center

U_{max} Maximum test section flow speed

w_{ts} Test section width

X_C Normalized downstream distance from contraction inlet

x_C Distance from contraction inlet

y_C Radial distance from contraction centerline at x_C

y_{CI} Radial distance at contraction inlet

y_{CO} Radial distance at contraction outlet

List of Figures

List of Tables

Chapter 1

Water Tunnel Components and Instrumentation

1.1 Water Tunnels and their Applications

A water tunnel is the liquid equivalent of a wind tunnel. Both facilities use instrumentation to make fluid flow observations and collect valuable data from test articles. The data are used to paint a vivid picture of how bodies influence the flow and vice versa. Wind tunnels make observations in air flow and have been used in situations that range from measuring the drag and lift of airfoils [1, 2] to observing the aerodynamic characteristics of a missile in supersonic conditions [3]. Water tunnels have been used to observe and record hydrodynamic loads to visualize the flow [4], and to study cavitation [5, 6, 7]. Water tunnels are specialized pieces of equipment; as a result, they are often designed and constructed to meet a specific use. Refs. [7, 8] detail tunnel design and construction for distinct flow conditions.

Water tunnels can also be used to assess the hydrodynamic response of submerged bodies as they interact with the flowing fluid. Hu, Lu, and He studied the hydroelasticity of hydrofoils in Ref. [9]. Their experiment involved the use of water tunnels to assess the deformation, lift, and twist angle of the hydrofoil as they varied the Reynolds Number and initial incident angle in non-cavitating flow. In cavitating flow, the vibration amplitude and response frequencies of the hydrofoil are evaluated. Daily [10] used water tunnels to obtain pressure distributions over submerged bodies and analyzed the hydrodynamic behavior of various jet-propelled or internal combustion propelled devices. The marine industry recently began generating interest in the use of composite materials as a means of replacing traditional manganese-nickel-aluminum-bronze (MAB) or nickel-aluminum-bronze (NAB) propellers. In a study involving propellers made from composite materials, Young used water tunnels to validate and compare theoretical predictions for strength-to-weight and stiffness-to-weight ratios with experimental results [11].

Tables 1.1 and 1.2 list high speed water tunnels around the world and their ownership. The tables provide test section dimensions and allow for the comparison of tunnels using mass flow rate and speed. Table 1.1 lists tunnels with a rectangular cross section, while Table 1.2 lists tunnels with a circular cross section. Among high speed water tunnels owned by academic institutions within the United States, there are only four tunnels that rank above the UGA tunnel in terms of mass flow rate.

Table 1.1: Partial list of high speed water tunnels with a rectangular cross section around the world organized by mass flow rate.

Tunnel	Location	Test Section Size Rectangular W (m)	H (m)	L (m)	Max Mass Flow Rate (kg/s)	Max Speed (m/s)	Reference(s)
Large Cavitation Channel (LCC)	US Naval Surface Warfare Center - Carderock (USA)	3.05	3.05	13	167,445	18	[12]
LOCAT	Korea Research Institute of Ships and Ocean Engineering - KRISO (Korea)	1.80	2.80	12.5	75,600	15	[13, 7]
Flow Noise Simulator (FNS)	Naval Systems Research Center (Japan)	2	2	10	60,000	15	[14]
HYKAT	HSVA (Germany)	1.60	2.80	11	53,760	12	[7, 15, 16]
Grand Tunnel Hydrodynamique (GTH)	Bassin d'Essais des Carènes (France)	1.10	1.10	6	24,200	20	[17]
Medium cavitation tunnel	HSVA (Germany)	0.57	0.57	2.20	3,087	9.5	[18]
Mini-LCC	University of Michigan (USA)	0.22	0.22	0.93	1,210	25	[19]
ARL 12-inch Water Tunnel	Applied Research Lab at Penn State (USA)	0.11	0.51	0.76	1,178	21	[20]
UGA Water Tunnel	University of Georgia (USA)	0.30	0.30	1	1,017	11.3	Current Thesis
St. Anthony Falls High-Speed Water Tunnel	University of Minnesota (USA)	0.19	0.19	1.30	722	20	[21, 22]
Tunnel de Cavitation	Ecole Navale (France)	0.19	0.19	1	542	15	[21, 23]
High-Speed Cavitation Tunnel (HiCaT)	University of New Hampshire (USA)	0.15	0.15	0.91	293	13	[7]
OSU 6-inch Water Tunnel	Oklahoma State University (USA)	0.15	0.15	1	225	10	[19, 8]

Table 1.2: Partial list of high speed water tunnels with a circular cross section around the world organized by mass flow rate.

Tunnel	Location	Test Section Size Circular Diameter (m)	L (m)	Max Mass Flow Rate (kg/s)	Max Speed (m/s)	Reference(s)
Garfield Thomas Water Tunnel	Applied Research Lab at Penn State (USA)	1.2	4.30	20,697	18.3	[24]
36-inch Variable Pressure Cavitation Tunnel	US Naval Surface Warfare Center - Carderock (USA)	0.91	4.51	16,715	25.7	[25]
Large high speed cavitation tunnel	HSVA (Germany)	0.75	2.25	8,615	19.5	[26]
24-inch Variable Pressure Cavitation Tunnel	US Naval Surface Warfare Center - Carderock (USA)	0.61	0.55	4,968	17	[27]
ARL 12-inch Water Tunnel	Applied Research Lab at Penn State (USA)	0.30	0.76	1,484	21	[28, 29]
Ceccio 9-inch Water Tunnel	University of Michigan (USA)	0.23	1.10	748	18	[30, 21]
12-inch Variable Pressure Cavitation Tunnel	US Naval Surface Warfare Center - Carderock (USA)	0.30	0.30	516	7.3	[31]
ARL 6-inch Water Tunnel	Applied Research Lab at Penn State (USA)	0.15	0.64	424	24	[32]
Ultra-High-Speed Water Tunnel	Applied Research Lab at Penn State (USA)	0.04	0.10	105	83.8	[33]

1.2 Design Elements of Water Tunnels

Water tunnels are composed of several components that play an integral role in the performance of the tunnel. Key components of water tunnels include the pump, motor, diffuser, contraction cone, flow conditioner, turning vanes, and the test section [34]. In a recirculating tunnel, water follows a circuit that begins at the pump and flows through the corners, flow straighteners, contraction cone, test section, diffuser, and around the corners before returning to the pump. The design of each component is especially crucial, because flow disturbances at any point within the tunnel can affect the flow characteristics in the test section. The University of Georgia water tunnel uses a boat propeller driven by a motor as its pump system. Most of the UGA water tunnel has a square cross section. The portion that contains the propeller is circular and is connected to the rest of the tunnel using cross-sectional transitions.

1.3 Water Tunnel Instrumentation

1.3.1 Qualification

The purpose of the water tunnel qualification is to quantify the flow field in the test section. Considerations must be made at the beginning of designing the tunnel for data measurements to be taken, for example, a laser based system for measurement requires the test section to be made of a transparent material, while a pitot tube system allows for more limited optical access. There are many systems available for qualifying fluid flow. Some of the more common systems include pitot tubes, hot wire anemometry, Laser doppler anemometry (LDA), and particle image velocimetry (PIV). Pitot tubes have been around since the early 18th Century [35]. They are a crude and cheap instrument, but can produce accurate measurements when properly calibrated. Hot wire anemometry makes use of heat transfer principles. The probe at the tip of the anemometer is heated and measurements for flow velocity are calculated as the current supplied to the probe varies to accommodate the speed of the fluid. LDA systems, which will be discussed in Section 3.1, measure the velocity of particles transported by flow. PIV systems obtain instantaneous velocity vector measurements of tracer particles in a cross section of flow [4].

1.3.2 Pitot Tubes

A pitot tube system, normally composed of the tube, a differential pressure transducer, and a computer/software system, can be used to produce accurate measurements for velocity and volumetric flow rate of a fluid. As the fluid flows through and around the pitot tube, a signal is generated by the differential pressure transducer. That signal is a measurement of the difference between the total pressure and static pressure. The total pressure is the result of the combination of the static (or atmospheric) pressure and the pressure generated by the flowing fluid. The difference between total and static pressure is the magnitude of the fluid's velocity pressure. From there, the velocity of the fluid is calculated using the density of the fluid.

Two pressure ports are located at the top of the tube. One tube measures the static pressure while the other measures the total pressure [36]. The sensing tip is located at the bottom of the tube. The sensing tip is positioned such that fluid flows towards the opening. The tube is designed to be co-axial, meaning that the pitot tube consists of an inner tube and an outer tube. The inner tube is used to measure the total pressure from the sensing tip, while the outer tube is used to measure the static pressure [36]. The shape and location of the sensing tip of the pitot tube are often redesigned to correct errors that may occur while reading system pressures. The tip design preference is based on requirements for cost and performance.

In the past, manometers have been used to measure the differential pressure within pitot tubes, but computerized data acquisition systems in conjunction with some type of differential pressure sensor have come to replace them. As fluid flows over the pitot tube, the pressure sensors record an electrical signal proportional to the system pressure, which a computer system translates to velocity measurements. To obtain accurate measurements, the opening of the tube must be designed to reduce flow turbulence. The velocity must be within a specified range for the data to be reliable and accurate. Placement of the pitot tube is also extremely important in obtaining accurate measurements. The pitot tube must be placed in the test section so that the sensing tip is aimed directly into the flow stream. The ideal placement of the sensing tip is at the average velocity point in the flow stream [36]. The tube system must also be properly calibrated for the flow readings to have any type of significance. The flow of the system must already be known, calibrated, and traceable. The calibration procedure will produce a calibration curve that plots pressure drop versus the flow rate. Pitot tubes have advantages with respect to simplicity and ease of use. They also provide an excellent method of velocity measurement when optical access is limited.

1.3.3 Hot-Wire Anemometry

Hot-wire anemometry functions using principles of heat transfer. It is used to measure the velocity and turbulence of fluid flow. An electrical current is run through the hot wire probe. In general, there are two types of hot wire anemometers: constant temperature and constant current. Constant temperature anemometers attempt to maintain the temperature of the probe by varying the current flowing through it [37]. Constant current anemometers, however, maintain the current being applied to the probe regardless of flow conditions. As the fluid flows over the anemometer, it will absorb and carry away some of the heat being generated by the probe, cooling the wire. When properly calibrated, the anemometer uses the rate of heat transfer and an energy balance equation to determine the velocity of the flow. Many different types of hot-wire anemometers exist. The construction of a hot wire probe may include one, two, or three sensors that allow for calculations involving one-, two-, or three-dimensional flow [37]. Each sensor is either constructed of a wire suspended between two prongs or a thin metal film deposited on an electrically insulating substrate. The wire is generally made with tungsten, platinum, or platinum-iridium and may be coated with gold or quartz. The material selected, the diameter of the wire, and the type of probe all depend on the intended use of the anemometer [37]. In the case of a constant current anemometer, if the rate of heat transfer is too slow to properly cool the probe, it faces the risk of overheating and burning out. The constant current anemometer also faces the potential complication of poor flow measurements at high flow speeds since the current may no longer be able heat the probe sufficiently [37]. As a result, constant temperature anemometers are generally preferred.

1.3.4 Particle Image Velocimetry

Particle image velocimetry (PIV) is another optical flow measurement method. The design of a PIV system generally makes use of tracer particles added to the flow. The system uses a laser to illuminate the tracer particles in a plane of flow. A laser is shined through a light sheet that generates the plane. The particles must be illuminated at least twice in a short time interval. The light is scattered by the particles and displacement is recorded and evaluated by a high-quality lens. When done on a single frame, a high-resolution digital or film camera is generally used. When done on two separate frames, special cross-correlation digital cameras are used. The system works on the assumption that the particles are moving with the local flow velocity between illuminations. The image is developed, then the photographical PIV recording is digitized, then transferred to the computer [4].

The illumination plane of the PIV image is broken down into subareas known as interrogation areas. Assuming all particles within an interrogation area homogeneously, the local displacement vector for the images of the particles between illuminations is determined using statistical methods, including auto- and cross-correlation. The statistical methods account for the time delay between the two illuminations and the magnification of the image. The result is a two-component velocity vector for the particles within the interrogation area. The process is then repeated for each interrogation area within the recording.

Modern charged coupled device cameras have the ability to capture about 100 PIV recordings per minute while a high-speed recording on complementary metal-oxide semiconductor sensors can capture recordings on the kHz range. It takes a standard computer about one second to process one PIV image with several thousand instantaneous velocity vectors [4]. Faster processing speeds are possible at the expense of precision.

PIV, like laser Doppler anemometry (LDA), has the advantage of being non-intrusive. This creates the ability for measurements in high-speed flows with shocks or in boundary layers close to the wall. This is not possible in intrusive systems using pitot tubes or hot-wire anemometry since the presence of probes may disturb flow. As with LDA, the velocity measurements are indirect. PIV measures the velocity of the tracer particles within the flow. One advantage that PIV systems have over all other systems listed is that PIV records images of large parts of the flow field. Most other qualification techniques can only measure velocity at a single point. This allows PIV systems to detect spatial structures, even in unsteady flows.

The use of tracer particles comes with many limitations. The particles must be small enough to accurately follow fluid flow. For PIV, particles must also be large enough to be effectively illuminated. Large particles scatter light better than small particles. They are easier to trace in flow, making it possible to lower peak power required from light sources. The duration of illumination must be short enough to freeze the motion of the particles and the time between the two illuminations must be long enough to determine the displacement between the particles [4].

PIV can be used to record the motion of the particle as it follows fluid flow. PIV directly uses a cross section of flow to measure instantaneous velocity and indirectly visualize flow. PIV is ideal for unsteady aerodynamic flow. PIV software allows for the photographic recording of micro-particles as they move through the established cross section.

1.3.5 Force Balance

To measure the hydrodynamic forces on test articles, a force balance is used. Force balances often use strain gauges to measure hydrodynamic forces and moments. A force balance is typically comprised of flexural components. As water flows through the tunnel, forces act on the model and create strain in the flexural elements. The strains are converted into electrical signals by the strain gauges. The strain gauges are generally wired using a Wheatstone bridge circuit. The magnitude of the electrical signal recorded by the strain gauge is proportional to the magnitude of the force. When properly constructed and calibrated, this relationship creates an accurate estimation for the forces and moments applied to the test model [38].

A force balance can be constructed to measure between one to six components of forces and moments; the forces include lift, drag, and side, while the moments include pitch, roll, and yaw. To accurately measure each component, the wiring scheme must be properly designed. Each element must be capable of independently measuring a specific component of force and moment while minimizing interactions with other components. The separation of components and linearity of the force balance are factors that are crucial at each stage of design, fabrication, and calibration. During design, separation and linearity are affected by the selected materials, spatial dimensions, and the shape and form of the structure. One design consideration regarding materials is the fact that same materials exhibit different hysteresis responses, meaning the recorded value for strain may lag behind the physical change at different rates in the different components. Proper selection of the elastic material and sensor may help to minimize these effects. There are many criteria surrounding the proper structural design of a force balance, but the importance of each criterion is relative depending on the type of balance and its intended use. Some of the criteria for design considerations include: the limits on the dimensions of the model, the ranges of forces and moments that the balance is expected to measure, the ability to measure large strains while retaining sensitivity and considering a reasonable factor of safety, high stiffness in the flexural elements, minimal deflection, uniform strain at key measurement points, simplicity in machining and installation of strain gauges, and high strength and low hysteresis of the system [38].

1.3.6 Flow Visualization

Flow visualization is an important consideration when attempting to understand fluid flow and fluid-structure interactions. Flow visualization is the process of making the motion of fluids, generally invisible to the human eye, visible for direct observation. Flow visualization methods can be static or kinetic, with each method having its own set of advantages. Static methods help to observe the velocity gradient at the surface of a solid boundary. They also help to specify regions of transition and separation of the boundary layer. Kinetic methods make use of tracer particles or bubbles. These methods can be used to observe three-dimensional flow. Flow visualization as a whole is used to observe flow phenomena that arise as a result of viscous effects, vortices, separation, etc. It is also used to verify hydrodynamic theory [4, 39].

Flow visualization can be achieved using three distinct approaches: adding foreign material to the fluid, optical methods, and methods that involve adding heat or energy. Visualizations that involve adding foreign material, also known as non-optical methods, include visualization with tracers; foreign material can be added through photo-chemical production of tracers, electro-chemical production of tracers, injection of tracers, smoke, dye, air and hydrogen bubbles, powder, fog, etc. Optical methods include the shadow method, Schlieren method, interferometry, electronic speckle interferometry and shearography, laser Doppler anemometry, and particle image velocimetry. Special methods that add heat or energy include energy adding, refractometry, and the use of a laser light sheet.

Flow visualization can also be broken down into surface flow visualization and off-the-surface visualization. Surface visualization includes tufts, fluorescent dye, oil, and special clay mixtures. Off-the-surface visualization includes tracer as smoke particles, oil droplets, and helium-filled soap bubbles. Surface flow visualization provides information about the boundary layer, transitions, flow separation, whether flow is laminar or turbulent, etc. Off-the-surface flow visualization provides information about the entire flow field. Both visualization techniques require sufficient lighting and some type of device for recording the flow field [4].

1.3.6.1 Water Tunnel Visualization Methods

Dye injection is a visualization technique that can be used within a water tunnel and is generally considered to be one of the simpler methods. The dye is injected using a small ejector tube or from small orifices. When selecting a dye for flow visualization, food coloring, aniline, methylene, potassium permanganate, ink, and fluorescent dyes can all be used but are generally mixed with alcohol or milk [4]. The milk gives the dye high contrast when being mixed with a flowing fluid and the alcohol helps to maintain the specific weight of the flowing fluid in rotating flow. Choices for color are made from personal preference, but reds, blues, and greens tend to produce better picture contrast. Dye is not a good choice for turbulent flow visualization because the flow causes the filaments to decay and the dye to mix with the fluid. Dye used in a water tunnel with a closed loop will progressively contaminate the water [4]. This creates the added requirement that the tunnel be drained and cleaned or filtered after each dye injection. When using a photo-active solution (pyridine dissolved in ethyl alcohol or nitrospyran in kerosene) as the dye for visualization, it is possible to produce electrolytic and photo-chemical reactions [4]. The photo-chemical reaction can be triggered by focusing a light from a flash tube or a pulsed ruby laser at a point in the photo-active solution. This resulting reaction produces a spot of blue dye that can be used for both flow visualization and velocity profile measurements.

Tracer particles can be solid, liquid, or gaseous, but must be moving at the same velocity of the fluid. The particle must be spherical with a diameter between 0.1 and 20 µm [4]. The particles chosen need to be as small as possible. This is because the smaller the particle, the better it approaches the speed of the flowing fluid and because particles of finite size and mass cannot follow abrupt changes in motion. The particles chosen should also be non-corrosive, non-toxic, and highly reflective. To allow the particle to approach the velocity of the flowing fluid, it is a necessity that the particles are injected into the system far enough upstream of the test section. Photographic images of the particle are taken at a set exposure time or an exposure of the entire flow field is taken. Each particle will be reproduced in the image with a streak of finite length [4]. The displacement, or streak, of the particle when divided by the time of exposure, can be used to obtain a measurement of the velocity of the particle or of the vector field.

Gas bubble visualization, specifically hydrogen bubble visualization, has been an instrumental technique when it comes to understanding fluid dynamic phenomena. Hydrogen bubble visualization has been used to establish fundamental understanding in boundary layers, turbulence, separated flows, and wakes [40]. Hydrogen bubble visualization uses electrolysis to create material sheets and timelines of minuscule hydrogen bubbles. The bubbles, when properly illuminated, create a vivid depiction of the flow field. When captured using visual techniques, they can also be used to obtain quantitative data. A conductive wire attached to a metal or carbon electrode are used to establish the DC circuit responsible for generating the hydrogen bubbles. The length of the conductive wire generally falls between 25 and 50 µm. The wire is established as the negative electrode while the metal/copper is the positive side. Hydrogen bubbles that are between half to the full length of the wire form on the wire due to electrolysis and are carried off in the direction of the flow. If the charge on the circuit is reversed, oxygen bubbles form on the wire instead. The hydrogen bubble wire probe can be installed anywhere in the flow field at any orientation and still be an effective visualization tool. It is important to note that the technique is generally more effective for flow with a low Reynolds number, and if the wire probe is placed too far away from the test section, the bubbles will disappear before visualization can occur.

1.4 Contributions

This thesis documents the design and fabrication of the UGA water tunnel and the justifications for design decisions. Sources of relevant information and calculations that were used to obtain design parameters are included. Drawings of the major water tunnel components were compiled and included in Appendices A and B. The thesis also documents the qualification of the UGA tunnel; the qualification and deaeration procedures are recorded. After the qualification of the tunnel, the results were recorded and processed. The processed data were used to generate the the figures shown in Chapter 3. The figures are discussed and show that the flow is well behaved across a large range of flow speeds. As a graduate researcher, I was responsible for compiling and recording the details of the tunnel's design, which had not been properly recorded in one source until now. I also completed the qualification of the tunnel, which involved learning how to use and program the laser doppler anemometry system, using the laser to collect flow data, analyzing the data, and using this analysis to create the figures in Chapter 3, and concluding that the tunnel generates uniform, laminar flow within the test section.

Chapter 2

Design and Construction

Literature concerning existing water tunnels was used as the foundation of knowledge for the design of the current tunnel. Design criteria were generated and presented to the Instrument Design & Fabrication Shop at the University of Georgia. The initial criteria were based on test section size, the contraction ratio, desired maximum speed, and overall size constraints. An examination of the University of Michigan facility, which houses the Mini-LCC and Ceccio 9-inch Water Tunnel, provided insight on additional design considerations and proper maintenance of the future facility.

The design inputs for the tunnel included a test section width (w_{ts}) and height (h_{ts}) of 30.48 cm, length (l_{ts}) of 1.00 m, cross-sectional area (A_{ts}) of approximately $929\,\mathrm{cm}^2$, maximum flow speed (U_{max}) of 10 m/s, minimum contraction ratio (r_c) of nine, and a minimum pressure (p_{min}) of 101 kPa. Assumed quantities included an energy ratio (r_e) of five, water temperature (T) of 20°C, and water density (ρ_w) of $1000\,\mathrm{kg\,m^{-3}}$. The energy ratio, defined as the ratio of system energy output to system energy input, was selected to account for fluid losses in power calculations, as computed in similar tunnels [41].

Using these values, water vapor pressure, p_v is,

$$p_v = 10^{\left(A - \frac{B}{C+T}\right)} Tr = 2,330 Pa, \tag{2.1}$$

where A = 8.07, B = 1,731, C = 233.43, and Tr is the conversion factor between Torr and Pa, 133.32—all values are obtained from the Antoine equation [42]; the cavitation number [43], Ca is,

$$Ca = \frac{(p_{min}\rho_w) - p_v}{(0.5)\rho_w U_{max}^2} = 1.97. \tag{2.2}$$

The cavitation number is a dimensionless number that expresses the ratio of the difference between absolute and vapor pressure and the kinetic energy per volume; it is useful for determining when cavitation may occur in a flow. As velocity increases, the cavitation number decreases, increasing the chance for cavitation to occur. The mass flow rate, $\dot{m}$ is,

$$\dot{m} = U_{max}\rho_w A_{ts} = 929\,\mathrm{kg\,s^{-1}}, \tag{2.3}$$

the power required without accounting for fluid losses P_{nl} is,

$$P_{nl} = U_{max}\rho_w A_{ts}^3 = 46,452W, \tag{2.4}$$

and the power required accounting for fluid losses P_{fl} is,

$$P_{fl} = P_{nl}\left(1 + \frac{1}{r_e}\right) = 55,742W. \tag{2.5}$$

$\dot{m}$ and P_{fl} were used to identify pump and power requirements respectively.

After accepting the proposal for the design and construction of the tunnel, the Instrument Design & Fabrication Shop faced major decisions surrounding the selection of materials due to cost constraints. Interaction between carbon steel and water would be detrimental to proper tunnel maintenance because of carbon steel's low corrosion resistance, so stainless steel was selected as the preferred material; with stainless steel being more expensive than carbon steel, minimizing material thickness for the structural components made from stainless steel was ideal. Strengthening ribs made from carbon steel were used to reinforce the structure and minimize stainless steel thickness. SolidWorks models were generated using the proposed arrangement, and the finite element analysis (FEA) package within SolidWorks was used to maximize structural integrity by altering material thicknesses of the stainless steel frame and carbon steel ribs to withstand anticipated pressures. The design of the tunnel was an iterative process, which began with the definition of the desired test section dimensions and maximum flow speed. A propeller was selected to drive the fluid in lieu of a pump to minimize cost. Bolt selection was based on minimum requirements for projected pressures and weights. The construction of the flanges was one of the largest challenges during construction of the tunnel; the size of the larger tunnel sections required each 91.44 cm side to be made separately before being fit together to form the flange. The remaining components were designed around the size and flow requirements of test section.

2.1 Design

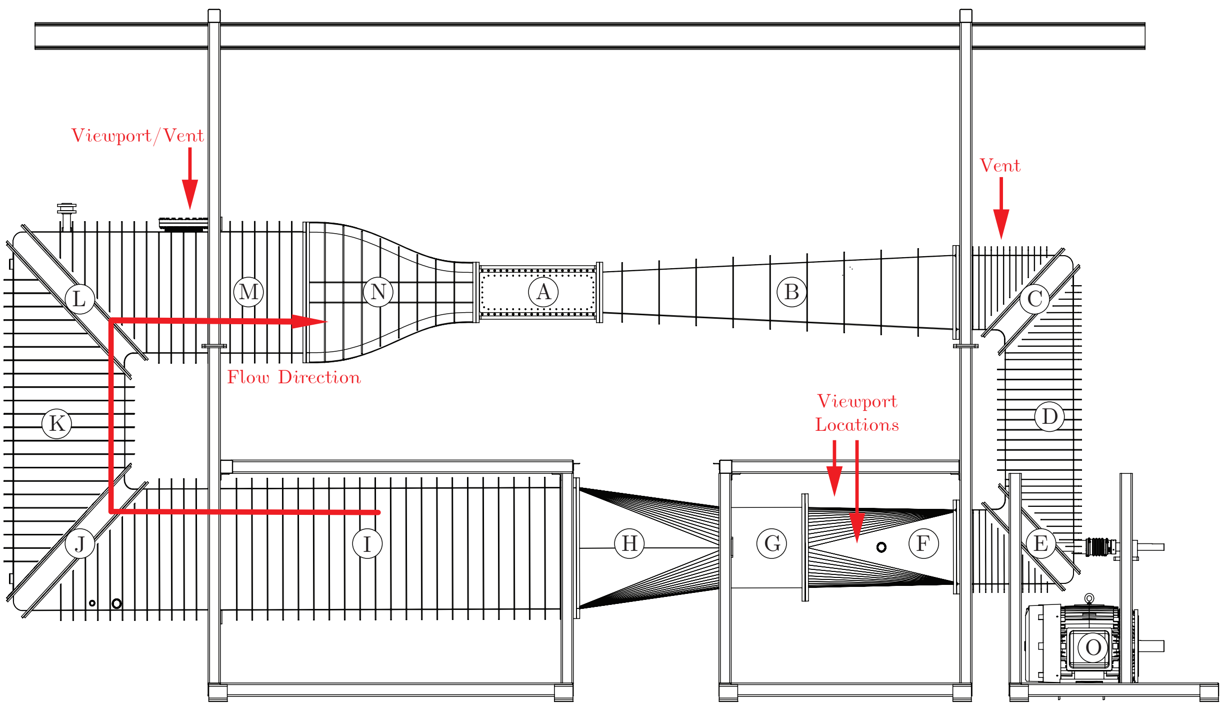

A.	Test Section	F.	Transition Section	K.	Settling Section
B.	Diffuser	G.	Propeller	L.	Elbow/Turning Section
C.	Elbow/Turning Section	H.	Transition Section	M.	Honeycomb
D.	Settling Section	I.	Settling Section	N.	Contraction Cone
E.	Elbow/Turning Section	J.	Elbow/Turning Section	O.	Motor

Figure 2.1: Overview of UGA water tunnel with labeled components

The design layout of the UGA water tunnel is shown in Fig. 2.1. Each of the major structural components is listed, and the design and construction of the majority of these components is described in the following sections.

2.1.1 Test Section

The test section is where models are tested and data are collected. Test section design is a significant consideration in the design of a water tunnel. The tunnel's intended uses affect decisions regarding the test section's cross section and size, which ultimately affect the cross section and size requirements for the entire tunnel. After determining the desired cross section and sizing requirements, numerous factors can be assessed, including flow speed, cavitation ranges, boundary layer growth, center line velocity, and blockage ratios [21]. Other constraints, such as the simplicity of installation and cost, must also be considered relative to the importance of each factor.

The size and shape of the test section must conform to its intended use. Viscous forces from the walls of the test section are responsible for boundary layer development due to the no-slip condition; as such, the inner surfaces of the tunnel should be as smooth as possible to minimize boundary layer thickness and blockage, among other properties. In addition, the thickness of the boundary layer is directly proportional to its distance from the contraction exit. As a result, there exists a practical limit for the length of the test section so that velocity profile remains as uniform as possible throughout the section [21].

The desired maximum speed must also be limited to minimize pressure requirements on the tunnel, because higher flow speeds require higher pressures to prevent cavitation. Higher pressure requirements may affect material choices and thicknesses for the test section. When considering typical instrumentation for data collection (e.g., a PIV or LDA system), the test section must be designed to have a sufficient optical access. Acrylic sheets fulfill this requirement, but extreme pressures within the test section require thick acrylic sheets or the selection of a stronger material, which can increase cost [21].

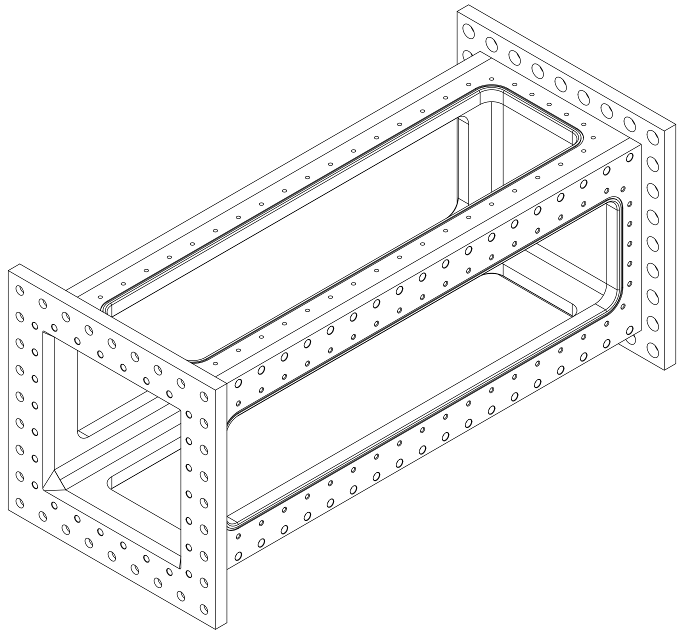

Figure 2.2: UGA water tunnel test section

Design of the test section, displayed in Fig. 2.2, is based on the redesign of the High-Speed Cavitation Tunnel (HiCaT) test section at the University of New Hampshire [7]. The frame is designed to fit the 1 m long and 30.48 cm square cross section sizing specified during the initial design phase. A SolidWorks model of the design was created and simulated using projected pressures to further identify safety requirements for the test section.

One consideration for the test section, observed from the Michigan Water Tunnel, was the need to avoid 90° corners in the test section. A transition in the corners helps to reduce turbulence in the boundary layer near the windows. Transitions were accomplished using mitered surfaces on the inner corners of the test section.

Acrylic was selected as the material for the test section window because it is a low-cost option that provides excellent visibility. The windows are machined to be interchangeable. A thickness of 5.08 cm, which provided a large factor of safety, was selected for the acrylic windows. The windows are cut to fit flush with the test section frame.

Screw sizes were selected to fit within dimensions identified from the SolidWorks simulation. The original design for the test section involved O-ring seals, and as a result, the screw heads needed to counter-bore inside the threaded holes. The number of screws are based on the projected pressures within the test section and the number of fasteners it takes to withstand those pressures using the section of plate available for sealing the test section. Selecting screw sizes for the sections in contact with the acrylic came with an extra consideration of the size of the screw head. The small head size of the cap screw creates a focused point for the pressure. To negate this effect, rather than use washers on each screw, a 3.2 mm thick stainless steel flange was cut using a water jet and placed around the acrylic to distribute the bolts loads evenly to the acrylic. The screws selected for the acrylic windows are 6.35 mm-20 thread size, 38.1 mm long, fully threaded stainless steel socket head screws. 48 screws in total are used to seal each test section window.

2.1.2 Diffuser

The diffuser decelerates high velocity flow exiting the test section while avoiding excessive energy loss or decreasing flow quality throughout the rest of the tunnel; in doing this, the diffuser regains pressure in the system. This goal is achieved through an increase in the flow's cross-sectional area. A gradual increase in the cross-sectional area aids in minimizing pressure losses in the system, but if the expansion half-angle is too large, flow separation may occur, resulting in high energy loss and flow instabilities that would ultimately create disturbances in the test section. If the half-angle is too small, it results in a diffuser too long to meet size constraints [44].

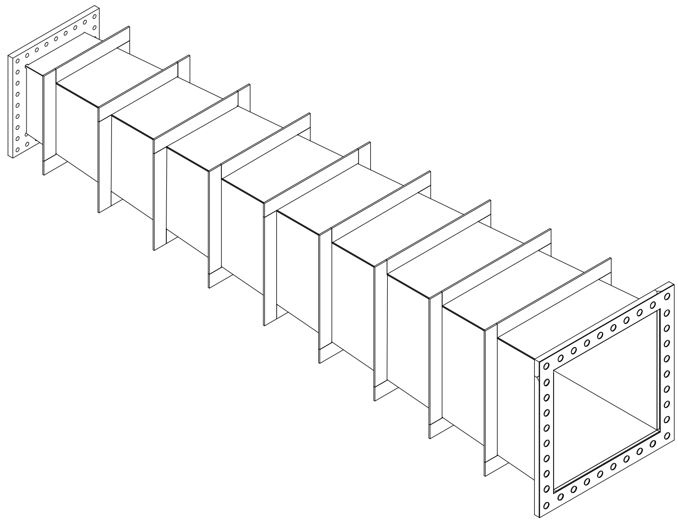

Figure 2.3: UGA water tunnel diffuser

Because the diffuser follows the test section in the flow circuit, its opening is the size of the test section. The diffuser outlet size was determined from flow requirements for the inlet of the propeller, which require a 55.88 cm square exit. The length of the diffuser was determined using the effective diffuser half angle, ϕ_{half}, in [7],

$$\phi_{half} = tan^{-1}\left(\frac{\sqrt{\frac{4a_{out}^2}{\pi}} - \sqrt{\frac{4a_{in}^2}{\pi}}}{2L_D}\right), \tag{2.6}$$

where a_{in} and a_{out} are the length of the side of the diffuser inlet and outlet respectively and L_D is the length of the diffuser.

A specified ϕ_{half} value of 3°, selected for the UGA tunnel diffuser, is within the acceptable range to prevent flow separation [21]. Using the confirmed values, a model of the diffuser was created in SolidWorks. This model was used in conjunction with SolidWorks's FEA package to determine the optimal material thickness for the diffuser walls and strengthening ribs. The diffuser was made to be approximately 3.05 m long and 3.2 mm thick.

2.1.3 Motor/Propeller

The purpose of the pump is to generate a pressure differential large enough to overcome the head losses in the system and drive the flow loop. To properly size the pump, an analysis of the total system head loss and desired volumetric flow rate is required [21]. The velocity and pressure ranges play a large role in determining the appropriate motor/pumping system. The maximum power of the motor sets the upper limit for tunnel speed; low speeds in a pump system result in poor flow conditions, but lower allowable limits allow for greater variability in the system's operating speed. Speeds below the pump's operation limit may result in pulsation or poor discharge velocity distributions.

The total static pressure is the sum of the test section pressure, the pressure difference in the diffuser, and the pressure difference resulting from the elevation difference between the top of the pump and the test section [21]. Cavitation is likely to occur within a pump at any flow rate if the static pressure is too low. At high flow speeds, the pressure regained within the diffuser may be high enough to prevent cavitation within the test section. Low flow speeds require a large change in elevation between the pump and test section to generate the necessary pressure difference [44]. While many tunnels are designed specifically for cavitation experiments, cavitation is generally unwanted because it can cause flow non-uniformity and acoustical interference [21].

Calculations shown in Section 2 were used to determine the power requirements for the motor and mass flow rate for the propeller. The flow rate was determined by multiplying $\dot{m}$, calculated in Eq. (2.3), by the mass flow rate conversion ($\dot{m}_c$ = 15.81 gpm/kg/s) to obtain a flow rate of approximately 946 L/s. Total developed head of the system was determined to be approximately 10.06 m at 10 m/s. A value of 12.19 m for developed head was selected to increase the margin of error for calculations. At 10 m/s, the system requires a 60.96 cm pump, 60.96 cm return line, and 91.44 cm exit line. Calculations show that a 5.574×10^4 W motor is the smallest that can successfully fulfill these requirements; a 9.321×10^4 W motor was selected for convenience.

Because cost was a major constraint, a propeller was viewed as more practical than a pump. The size and pitch of the propeller were based on a desire for approximately 900 RPM using a 9.321×10^4 W motor assuming 75% efficiency. The propeller, made of bronze, is connected to a piece of zinc that acts as a sacrificial anode. Sacrificial anodes are less noble and highly active metals that prevent corrosion of the more noble and less reactive metals. The propeller has four blades designed for right hand rotation with a diameter of 58.42 cm and a pitch of 63.5 cm.

2.1.4 Contraction Cone

The primary purpose of the contraction cone is to minimize turbulence while increasing flow speed. The inlet to outlet ratio, also known as the contraction ratio, greatly affects the cone's effectiveness in minimizing the increase in turbulence. Greater contraction ratios lead to lower turbulence and therefore a more uniform velocity profile within the test section. Furthermore, a high contraction ratio consequently increases the associated construction costs, because a bigger contraction results in a larger tunnel. A large contraction inlet lowers the resulting pressure in the test section, which may induce cavitation. Purdy and Straub [21] found that a contraction ratio of 9:1 provides a good design compromise between minimizing turbulence intensity and size constraints. The length of the contraction cone is also an important consideration; a long contraction cone results in a thick initial boundary layer in the test section, whereas a short cone causes the contraction to act as a backward facing step [21]. A backward facing step may occur when flow is subjected to a sudden increase in cross-sectional area. The sudden increase causes flow separation to occur at the point of expansion, which results in pressure loss, vibration, and noise within the system. In the case of the tunnel, the separation is a result of the sharp decrease in cross-sectional area and the shape of the contraction [45].

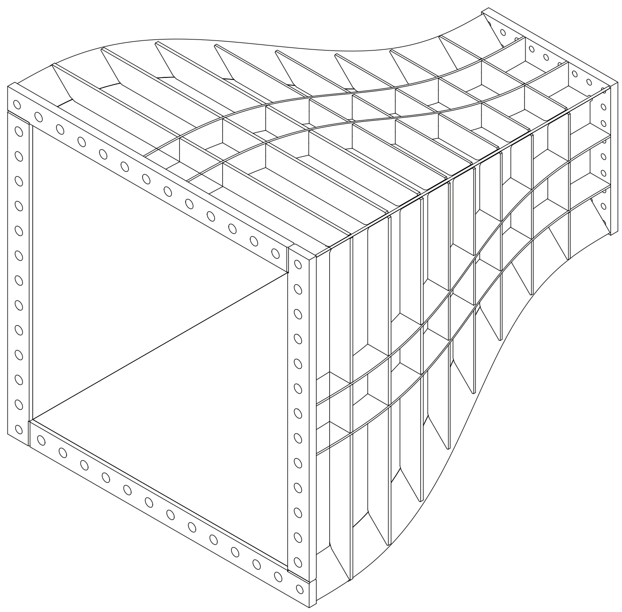

Figure 2.4: UGA water tunnel contraction

The design of the contraction cone, shown in Fig. 2.4, began with the desire for a 9:1 contraction ratio. Because the test section follows the contraction in the flow circuit, the contraction outlet is the same size as the test section, a 30.48 cm square. The 9:1 contraction ratio determined that the size of the contraction inlet would be a 91.44 cm square. The contraction requires a shape designed to speed up the flow while minimizing turbulence. A fifth-order polynomial, based on an analysis done for low speed wind tunnels [7], was determined to be the best shape to achieve the design requirements. The analysis was modified for water tunnels and has been used in the Large Cavitation Channel (LCC), HYKAT, and LOCAT. The fifth-order polynomial used to generate that shape is found in [7],

$$y_c = y_{CI} - (y_{CI} - y_{CO})(a_C X_C^5 + b_C X_C^4 + c_C X_C^3 + d_C X_C^2 + e_C X_C + f_C), \tag{2.7}$$

where L_C is the length of the contraction, x_C is the distance downstream of the contraction inlet, $X_C = x_C/L_C$ is the normalized distance downstream,y_c, y_{CI}, and y_{CO} are the radial distance from the center-line at a location x_C, the inlet of the contraction, and the outlet of the contraction respectively, and a_C, b_C, c_C, ..., f_C are the coefficients of the polynomial describing the contraction shape.

The design parameters were identified as follows: $y_{CI} = 45.72$ cm, $y_{CO} = 15.24$ cm, and $L_C = 137.16$ cm. These parameters were used in conjunction with Eq. (2.7) to generate the contraction shape, displayed in Fig. 2.5, in SolidWorks. The model, combined with SolidWorks's FEA package, was used to estimate required thickness for the contraction walls, 3.2 mm.

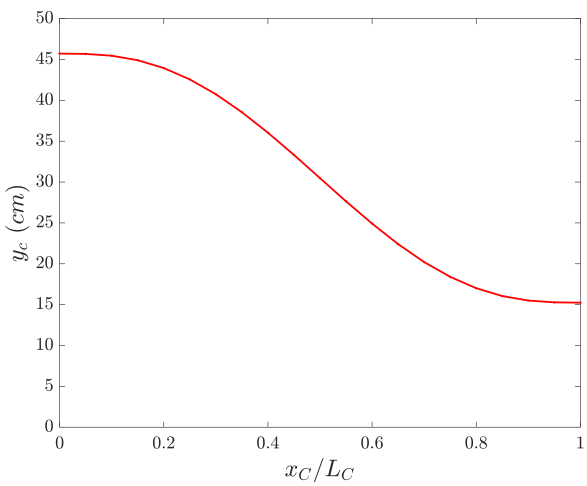

Figure 2.5: UGA contraction cone shape generated from Eq. (2.7)

2.2 Fabrication

2.2.1 Test Section Fabrication

The frame of the test section was built using a CNC milling machine. The working envelope of the mill is 1.02 m long, 0.51 m wide, and 0.64 m tall. Since the test section is one meter long, it was possible to machine the frame from one solid block of 304 stainless steel. After being machined, a water jet was used to blank all holes for screws and bolts, which were later machined to better fit the specified tolerances. The original design for the test section involved the use of O-ring seals on the mitered surfaces. It was later discovered that the O-ring seals were not a practical seal for the test section. The O-ring seals selected to seal the tunnel worked well initially, but wore down quickly as time went along. They became more difficult to secure in place and required higher compression to fulfill their function. As an alternative, all components of the test section were bolted together for mechanical integrity, and all seams were welded. The hermetic welds at the seams were used not for strength but to seal the test section.

2.2.2 Diffuser

The diffuser is made from two pieces of stainless steel bent at 90° angles, which were welded together to limit the number of weld seams and improve structural integrity. The inner surface of the diffuser is mirror finish stainless steel to reduce system losses due to viscous effects at the diffuser walls. The strengthening ribs surrounding the diffuser are made of carbon steel, and have no direct contact with water.

The strengthening ribs are 1.02 by 63.50 mm cold rolled flat bar carbon steel cut into four pieces to create each rib. Each set of ribs were then welded together and to the diffuser. The flanges of the diffuser were made from 25.4 mm thick stainless steel. The flange of the 30.48 cm end was machined from one solid plate, while the larger 55.88 cm exit was assembled from four plates that were cut, beveled, and welded together. The pieces of each flange were fixed on a mill where holes were drilled before machining and welding occurred. A welding fixture was created to align the components and bolt holes during welding to prevent shifting during the process. The flanges were then welded to the diffuser.

2.2.3 Corners/Turning Sections

The purpose of the turning sections, located in each elbow (corner) of the water tunnel, is to guide flow around corners while preventing the formation of turbulence, velocity disruption, and cavitation. There are many turning designs that can be used to achieve these results (e.g., radiused elbows, splitters, miter bends, etc.) [44]. An elbow with a radius that is too long or short results in poor velocity distribution after the turn; using splitters in these types of turns can help to improve velocity distribution and reduce the potential for cavitation. Miter bends composed of airfoil-type vanes are more compact than the previously mentioned solutions, while resulting in excellent flow conditions, low energy loss, and the elimination of cavitation. The design is one that has long been in use in aeronautics, but began to find favor in hydraulics in the late 1940s [44].

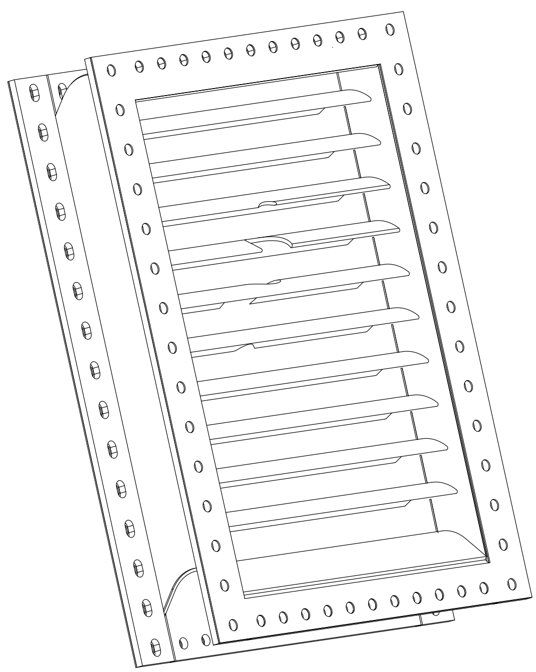

Figure 2.6: UGA water tunnel corner/turning section

The corners on the water tunnel are sized differently to accommodate flow requirements for the pump, diffuser, and contraction; as a result, two corners are 55.88 cm while the other two are 91.44 cm. The propeller requires a 55.88 cm inlet, while the contraction cone requires a 91.44 cm inlet to produce a 9:1 reduction for the test section. The two 55.88 cm follow the diffuser in the flow circuit, while the 55.88 cm corners are downstream of the propeller and just upstream of the honeycomb.

The turning vanes were created using 7.62 cm, schedule 40, stainless steel pipe. A fixture was created for the water jet to hold the pipe so that it could be cut into pieces that were 55.88 and 91.44 cm long before being quartered into four equal sections. The fixture also allowed for the pipe to be turned and indexed. Another fixture was made for the milling machine to cut the leading and trailing edges of the turning vanes. The leading edge was radiused so there would be a smooth transition as water flows into the turning section, while the trailing edge was made sharp to minimize trailing edge turbulence.

The number of turning vanes to be used in each turning section was determined by a SolidWorks model, which assessed the spacing of the turning vanes. The spacing started with a large gap of 15.24 cm between each turning vane and decreased to the point of diminishing return where adding more turning vanes no longer had a significant effect in reducing turbulence in the test section. It was determined that 7.62 cm center spacing was the optimal spacing for each turning vane.

2.2.4 Vertical Sections

As with the other components, the water jet was used for cutting the sheet stock that made the walls of the vertical sections. The sections of the walls were welded together. A saw was used for cutting the ribs, which were then assembled, welded together, then welded to the walls. The flanges were cut on the water jet, assembled, welded together, then welded to the walls.

2.2.5 Motor/Propeller

The assembly connecting the propeller to the motor begins with a pulley attached to the propeller shaft. The shaft moves through the turning vanes and into the transition section where the shaft is supported by a jaw coupling (also known as a spider coupling) which houses a cutlass bearing. The jaw coupling allows the cutlass bearing to be moved in four directions and and also has swivel that allows the bearing to turn for proper alignment with the propeller shaft. The shaft is sealed using a packless shaft seal (also known as a carbon-faced seal) which is commercially available for watercraft. The seal runs against a stainless steel collar that is fastened to the propeller shaft and has O-rings that seal it to the shaft. The seal uses an elastomer that, when in compression, exerts a force to overcome the pressure of the water, meaning it holds the carbon seal against the collar so the water is contained within the tunnel. Behind the carbon face seal, the shaft is supported by a pillow block bearing. The bearing gives radial support to the shaft and the overhung load of the pulley and motor.

2.2.5.1 Motor Belts

Preliminary designs to tension the motor belts involved the use of a spider coupling which would have been used to directly drive the motor; however, direct drive was not the desired propulsion mechanism for the motor. The water tunnel actually needed a speed reduction. The physical limitations of the room dictated that the motor shaft be parallel to the propeller shaft. The motor was then turned to conserve space which also allows it to be driven with sheaths. The number and type of motor belts required were based on the horsepower of the motor, torque requirements, projected speeds, and the diameters of the pulleys. The weight of the motor, 907 kg, was thought to be large enough for properly tensioning the belts, and as a result, the motor plate was hinged as a means of tensioning and un-tensioning the belts. The belts selected for the motor are 5VX1000 BANDO Power Ace Combo V-Belts.

2.2.6 Contraction Fabrication

As fabrication of the contraction cone began, the new challenge became forming the correct shape without scarring the surface finish. The inner finish of the contraction is important in reducing boundary layer turbulence entering the test section, so mirror finish stainless steel was selected to accommodate this requirement. From the shape generated in SolidWorks, a flat pattern was produced and cut using the water jet. This piece was used to bend and form the shape for the walls of the cone. When loads were applied to the 3.2 mm thick sheets, they began to deform outside of the acceptable boundaries, and since it would have been extremely difficult to form the contraction cone from anything thicker than 3.2 mm, the idea of an exoskeleton for the cone was developed.

The exoskeleton was made with linking slots, where a set of rails that are spaced for the length of the contraction and are shaped to the contraction profile. The rails have slots so that each bar that crosses the axis of the transition is slotted in the other direction. This allows the exoskeleton to fit together like a puzzle that holds itself together without any welds. Because the FEA modeling showed that the corners of the contraction were the weakest points, a plane was generated on a 45° angle that bisects the intersections of the corners and supports them like a brace. The ribs that pass through this point intersect that brace, which strengthens the overall structure without increasing the width or thickness of the ribs. The exoskeleton was used to form the walls of the contraction cone into the fifth-order polynomial shape while avoiding excessive deformation of the stainless steel. The walls of the contraction cone were welded together, and the flanges were welded on, as with the other sections of the water tunnel.

2.2.7 Flow Straightener/Honeycomb

As flow circulates through the tunnel, flow straighteners placed in each of the 90° bends can alleviate the effects of swirl and turbulence due to the turns. In general, some combination of screens, baffles, and/or honeycomb are used as well. Honeycombs are preferred in recent works [7, 8] for their ability to remove swirl from the flow and break up turbulent structures. Properly sizing the dimensions of the honeycomb will allow for a reduction of turbulence, as well as the minimization of head loss in the system. The disadvantage with using honeycombs is that each cell produces turbulence downstream. A settling chamber, which also necessitates sizing in relation to the honeycomb, can be placed downstream of the honeycomb to allow for a decay in turbulence within the flow exiting the honeycomb [21].

The casing and flanges for the honeycomb was constructed in a similar fashion to that of the rest of the tunnel. The main difference was that the walls were made to be 4.8 mm thick, rather than 3.2 mm like the rest of the tunnel. The length available for the honeycomb section and the desired spacing between the honeycomb and contraction cone determined where the honeycomb would be placed within the square section.

The honeycomb was sized to fit flush with the water tunnel shell. Even though a hexagonal shape is preferred because it eliminates spatial gaps, the cells for the UGA tunnel are 6.4 mm in diameter with a round shape due to cost constraints. The spatial gaps may allow fluid to pass through, creating additional cells that result in less uniform flow exiting the honeycomb. A PC2 polycarbonate honeycomb was purchased with 38.10 cm long cells that were cut down to 30.48 cm. It is desirable to have honeycomb cells long enough for flow within each cell to become fully turbulent [46]. While it may sound counter-intuitive, laminar flow exiting the honeycomb cells produce more turbulence due to the parabolic shape of the laminar flow profile. Turbulent flow, however, has a more uniform velocity profile that reduces the velocity and pressure gradients downstream of the honeycomb, ultimately resulting in less turbulent flow. Honeycomb specifications require that the honeycomb end 30 to 40 cell diameters before the contraction cone entrance, so the honeycomb was positioned 25.40 cm before for the contraction entrance.

2.2.8 Transition Section

The propeller requires a circular cross section to accommodate its rotation. To make this possible, the water tunnel transitions from a 55.88 cm square section to a 60.96 cm diameter circular section before returning to a 91.44 cm square. The housing for the propeller is solid pipe with flanges welded on. The transition section is 3.2 mm thick. The thickness was deemed appropriate for the projected pressures because the stainless steel was strengthened from the longitudinal bends in the transition. The transitions were formed and bent to fit the desired shape.

2.2.9 Horizontal Settling Section

The settling section following the propeller was difficult to construct due to its size and weight. The 91.44 cm square section was 3.05 m long, making it the longest section of the tunnel. It was made from four flat pieces welded together at the corners. Since the section was so long, the walls were 4.8 mm thick and ribs were added to increase the structural integrity.

2.2.10 Gaskets

Rather than purchasing the gaskets, they were made in-house. This decision was made to reduce the risk associated with purchasing stock material and gluing it, while saving on cost. The gaskets were made from a urethane mixture, which began to show embrittlement after installation. The cause of the embrittlement has not been identified even though the pressure is thought to be a factor. The urethane gaskets were discarded, and new gaskets, made of butyl (tire) rubber, were cut using the water jet and are being used in combination with silicone caulk. The new gaskets are 3.2 mm thick.

2.3 Water Tunnel Weight and Support Loads

The UGA water tunnel has a dry weight of approximately 5,900 kg and a wet weight of approximately 14,214 kg. This weight is supported on the tunnel's eight legs. To determine the distribution of weight across the tunnel's legs, the shape of the tunnel was divided into sections of basic shapes, and the centroid of each section was calculated. The shape of the contraction cone was modeled as a trapezoid for simplicity. It was assumed that the tunnel is symmetrical at the center of its width. The center of mass of the tunnel was determined from the centroid calculations. Force and moment equations were then solved to determine the weight distribution on the tunnel's legs. Calculations showed that all of the weight of the tunnel was supported between the two legs to the left of the contraction cone and the two legs to the right of the diffuser, as shown in Fig. 2.1. While wet, this results in a weight distribution of approximately 5,330 kg at each of the feet left of the contraction cone and approximately 3,280 kg at each of the feet right of the diffuser. The contraction feet have an area of approximately 1,240 cm^2 each, while the diffuser feet have an area of approximately

$180\,\text{cm}^2$. This results in a pressure distribution of approximately $420\,\text{kPa}$ at each one of the contraction feet and 1,810 cm^2 at each one of the diffuser feet.

Chapter 3

Qualification

This chapter discusses the qualification of the University of Georgia water tunnel. It explains the qualification process, discusses the instrumentation used, analyzes the data, and discusses its implications.

3.1 Instrumentation

Laser Doppler Anemometry (LDA) is the non-intrusive measurement technique used during qualification to measure the velocity of the flowing fluid. LDA functions by measuring the frequency difference between incident and scattered laser radiation of moving particles. It can do this by either tracking fluid particles or seeding particles inserted into the flow. The measured difference is a result of the Doppler effect. Many LDA systems use a dual-beam arrangement with forward-scatter light collection and burst-counter signal processing [47]. Measurements occur at the intersection of the lasers. The point of intersection contains an interference fringe pattern of alternating light and dark planes. As particles flow through the intersection, the particles scatter light on the bright interference planes. The fluctuations in light intensity are converted to electrical signals by a photomultiplier, which are then processed through a signal processor and converted to velocity information, shown in Fig. 3.1. Depending on the complexity of the LDA system, three components of velocity can be acquired simultaneously.

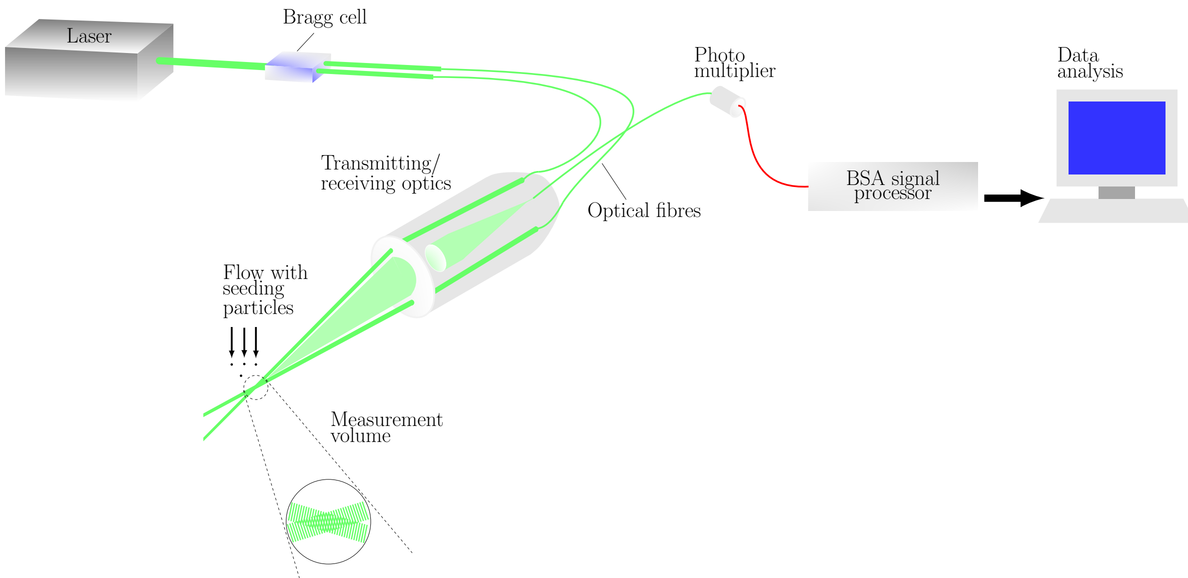

Figure 3.1: LDA system diagram

LDA has many advantages including the fact that it is non-intrusive. This means that the system can take flow measurements with little or no disturbance to the flow field. LDA systems that require a probe are still minimally invasive because the cross section of the probe is generally equal to the size of one of the laser beams. The main advantage of LDA is that calibration is not required. This is because the calibration constant is determined by the wavelength of the laser light and angle of intersection of the laser beams [48]. LDA systems can measure the normal or vertical velocity fluctuations close to solid surfaces, a measurement that is difficult for hot wire anemometry. LDA is also better than hot wire anemometry when measuring extremely turbulent flows.

LDA is not without its disadvantages, however. The method relies on micro-particles within the flow field to collect velocity data. The movement of the particles is measured, rather than the fluid itself. The assumption for this method is that the particles are small enough to follow the flow of the fluid exactly. Larger particles cannot keep up with fluctuations in fluid flow and may be unable to approach the velocity of the fluid. If the particles are not sufficiently small, measurement errors can arise. Problems may also arise if the particles are not uniformly distributed. It is often necessary for seeding particles to be introduced to the flow for more accurate flow measurements. If the intensity of the particle-scattered light is not high enough, it can cause delays in data acquisition. The photodetector may be unable to detect the scattered light due to the rapid fall off in scattered light intensities resulting from the small particle diameter [47]. Improvements in laser and photo-detection systems have helped to resolve many of the issues relating to scattered light reflection intensity.

LDA can also be a tool to indirectly visualize flow. The mechanics of small tracer particles are the same for LDA systems. If the particle is small enough, its velocity and turbulence is assumed to be the same as that of the flowing fluid. LDA uses laser anemometers as non-intrusive probes that have the ability to measure the instantaneous velocity and directional response of particles.

The LDA system obtained from Dantec Dynamics was the FlowExplorer DPSS System, mounted on a 3D traverse. The lasers in the FlowExplorer can be powered at 100, 150, or 300 mW at wavelengths of 532, 561, or 660 nm. The focal length, depending on the selected lens, can be adjusted to 300, 500, or 750 mm. The system is accurate for a velocity range of -150 to 650 m/s with a resolution of 0.002% of the selected velocity range and an uncertainty of 0.067%, with a coverage factor of two, which correlates to a 95.45% confidence interval for measurements based on the Student's t-distribution. The Student's t-distribution is a measure of the statistical significance of data and is defined as a ratio between a normal distribution with a mean of zero and the root mean square of k terms from the normal distribution, where k is the number of degrees of freedom [49]. The system can also read up to six million particle bursts per second.

3.2 Qualification Procedure

After extended periods of in-operation, deaeration of the water tunnel is necessary. The deaeration process was repeated precisely to maintain consistent operating conditions during qualification and to ensure the repeatability of results.

3.2.1 Deaeration Process

1. Overfill the tunnel slightly to balance water loss as the tunnel is deaerated.
2. Start the motor running at low speeds (5-10 Hz).
3. Let the motor run for about five minutes to allow the system to stabilize.
4. Ramp the motor up to a high speed (around 30 Hz).
5. While the motor is running at high speeds, slightly open the top vent behind the honeycomb. This will allow air bubbles to escape, but also carry some water out with it.
6. Allow step 5 to continue for 15-20 minutes.
7. Ramp the motor down to medium speed (around 20 Hz).
8. Repeat step five. Allow the tunnel to vent at lower speeds for another 10 minutes.
9. Ensure the water level in the tunnel is still full, but do not allow another air pocket to fill the tunnel. This can be done by slightly opening the vent and checking whether water flows out of the tunnel or air is sucked in.
10. Close the vent, and operate the tunnel as intended.

3.2.2 Qualification Process

The first step of the qualification process was to align the LDA system with the center of the test section. At this center point, the frequency of the variable frequency drive (VFD), starting at 0.9 Hz, was increased in 0.9 Hz increments until cavitation began to occur around 39.6 Hz. The cavitation became the limiting factor for tunnel speed. Higher tunnel pressures may have allowed the tunnel to reach higher flow speeds. The VFD frequency corresponds to the power delivered to the motor. The motor powers the propeller through a pulley system. The motor speeds corresponding to 1, 2, 5, 8, and 10 m/s were identified and chosen as the primary testing speeds. The stop criterion for each run was based on a 2% velocity root mean square (RMS) value, where RMS is defined as the square root of the arithmetic mean of the squares of a set of values. As data are collected, the velocity measurements converge towards a mean value until the variation in the mean value becomes negligible. All of the resulting data was then normalized to the baseline values during data processing.

To create a full map of the test section, a grid of points was generated for the LDA system. The points on the grid were generated so that there would be a dense area of grid points near the walls of the test section. A string of center line points was also taken for each axis to obtain a detailed line of points in each direction. The LDA system and its software were then configured for each run.

3.2.3 Limitations

When the lasers were oriented horizontally, they converged into the test section at an angle, which limited the area near the top and bottom of the test section where data could be collected. As a result, the laser had to be moved to a vertical orientation under the test section to collect previously out of reach data points. The horizontal data was collected with a 500 mm lens, while vertical data used a 300 mm lens. Program and traverse settings were adjusted to accommodate the change in focal length.

The X-direction of the traverse was limited to a total travel of 40 cm. The total length of the test section in the X-direction is 1 m. To cope with this limitation, the laser was shifted in the X-direction to the front of the test section. A grid that was less dense than the previous was generated for this new section. This configuration was completed for both the horizontal and vertical laser orientations. Time constraints prevented the back of the test section from being mapped out by the LDA system.

3.3 Qualification Data

This section discusses the data collected during the qualification process. The data are used to establish the operational capacity of the tunnel and affirm the quality of flow within the test section.

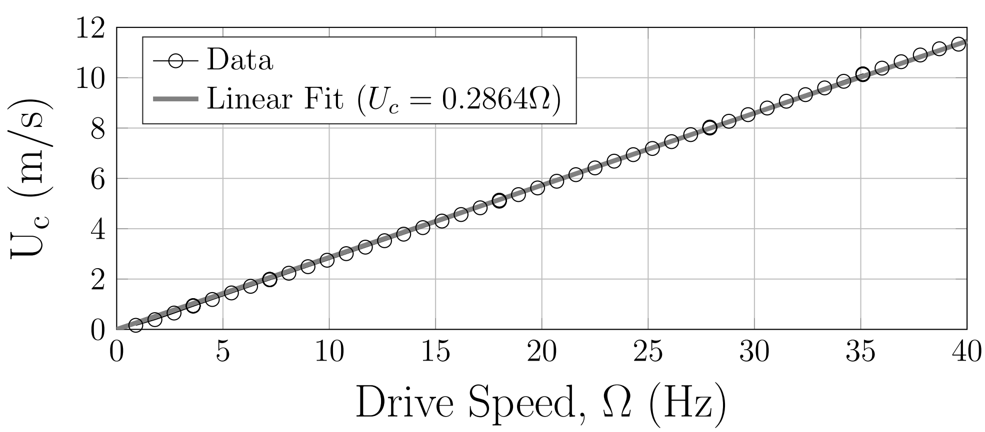

Figure 3.2: Flow speed vs. motor drive frequency at test section center

The water tunnel motor is driven by a VFD. The VFD displays motor speed in hertz. There was consequently a need to correlate the drive frequency and flow speed within the test section. To assess the repeatability of the measurements, data at the center of the test section from several independent qualification trials were included in Fig. 3.2. The independent data were consistent with data from the original trial. To assess the best fit of the data, a trend-line was fit to the points. Several linear and polynomial fits were tested. The polynomial fits did not significantly add to the accuracy of the curve. A linear fit ($U_c = 0.2864\Omega$), with the intercept set to the origin, was determined to be the best fit for the data (generating an R^2 value of approximately 0.9996).

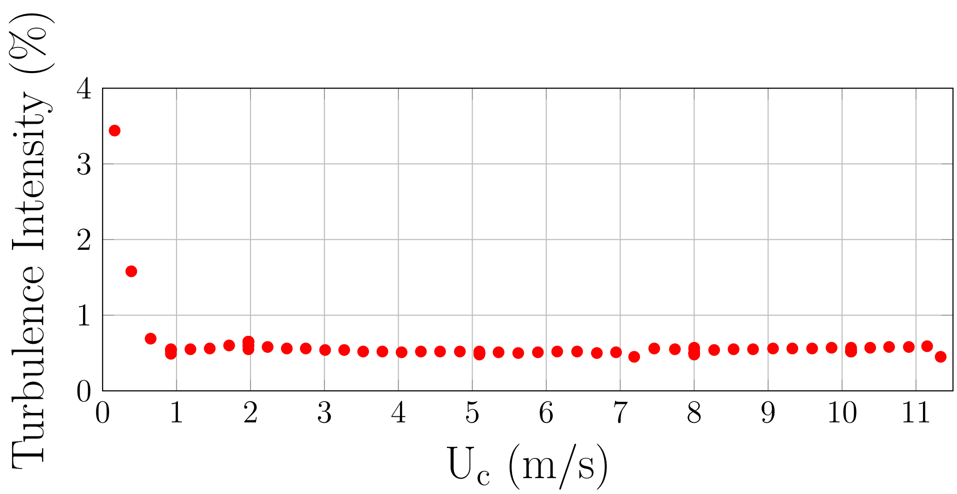

Figure 3.3: Turbulence intensity vs. flow speed at test section center

Flow speed and turbulence intensity data are collected at the test section center. Fig. 3.3 shows the turbulence intensity vs. flow speed. Flow speeds below 1 m/s show higher turbulence intensity, but above 1 m/s, the turbulence intensity is consistently near 0.5%. The turbulence intensity values for all data sets are defined as the root mean square of the velocity fluctuations divided by the average velocity of the data set; the velocity fluctuations increase with increasing flow speed, creating a percentage value of approximately 0.5% across all flow speeds. While the majority of the data for Fig. 3.3 was collected during one qualification test, several other data points at average values of 1, 2, 5, 8, and 10 m/s were collected from several other qualification tests and are included to show the repeatability of the data.

Fig. 3.4 shows dimensionless flow speed and turbulence intensity against the dimensionless position along the Z-axis of the test section. The flow speeds have been normalized to the

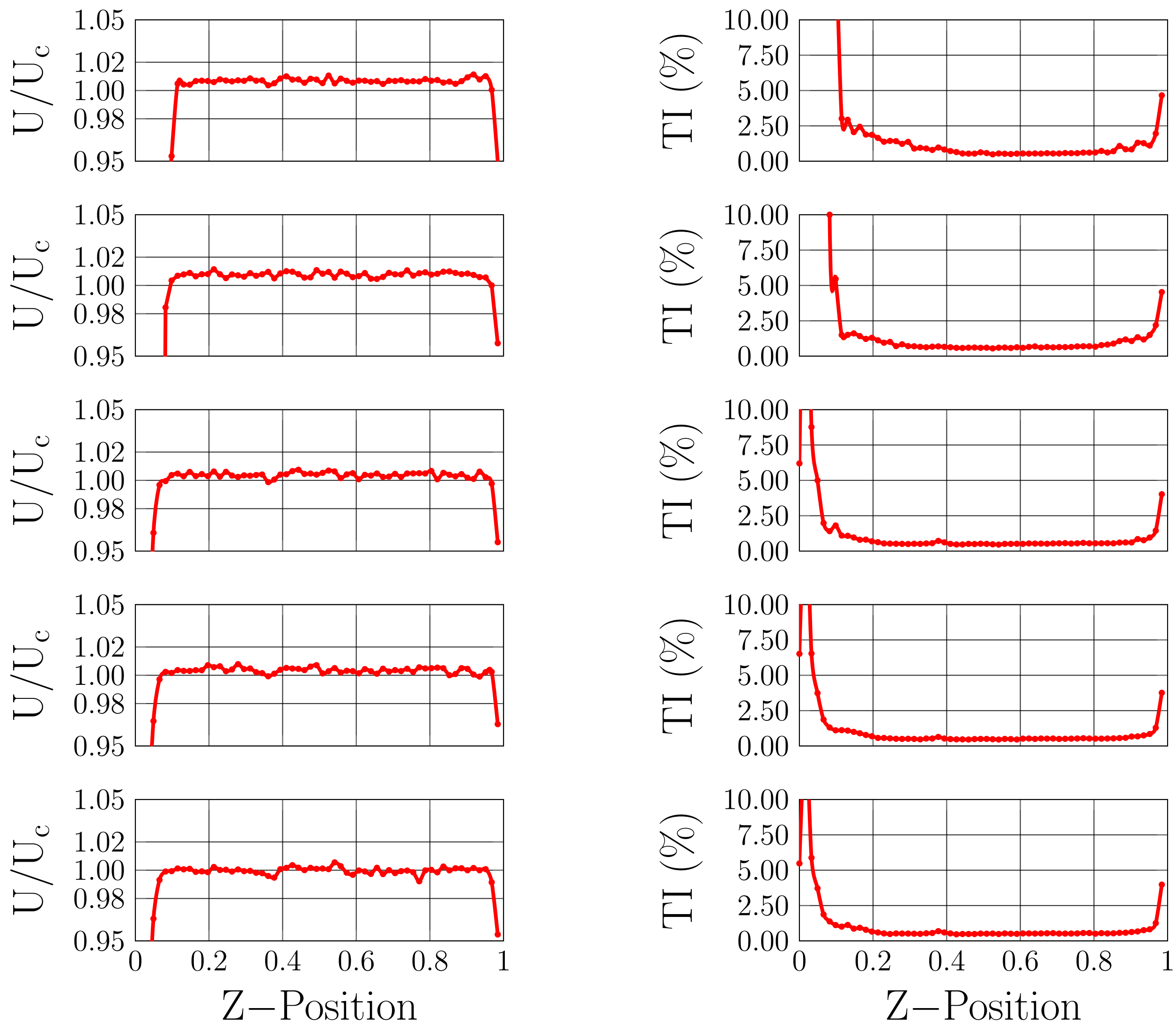

Figure 3.4: U/U_c vs. z−position at 1, 2, 5, 8, & 10 m/s respectively (left) and turbulence intensity vs. z−position at 1, 2, 5, 8, & 10 m/s respectively (right)

measured center point velocity (U_c) of each run. The Z-position on the X-axis has been normalized to unity, with one corresponding to the full length of the test section in the Z-axis (30.48 cm). The velocity profiles along the Z-axis show a uniform velocity distribution with small boundary layers. A similar observation can be made from the turbulence intensity plots. As distance from the boundary layer increases, the values for turbulence intensity drop to values of approximately 0.5%. Fig. 3.4 shows that flow speed fluctuations and turbulence intensities across the Z-axis remain fairly constant and low, at all tested flow speeds. A notable feature of the Z-axis is the asymmetry of the boundary layer, which can be seen in both the flow speed and turbulence intensity plots. This is likely a result of the 0.7° rotation of the test section, which occurred and was not detected during the original installation of the tunnel. The turbulence intensity data show high fluctuations between Z-position values of 0 and 0.1. Higher values for turbulence intensity are expected within the boundary layer, but the change in values from low to high and back to low (specifically in the 5, 8, and 10 m/s TI plots) is likely a combination of the tilt of the test section and laser interference at that point within the test section window.

Due to laser constraints, data collection in the Y-direction was extremely limited. As a result, only a few data points could be collected and used. Based on the limited data available for Fig. 3.5, findings regarding flow speed are fairly consistent with those in Fig. 3.4. The boundary layer thicknesses identified for the top and bottom of the test section are much larger than those identified in Fig. 3.4. The lack of data points in the Y-direction is likely the cause of this increase. Similar observations can be made for turbulence intensity. The maximum turbulence intensity values in Fig. 3.5 are much lower than those observed Fig. 3.4, which hints at the possibility of lower turbulence at the top and bottom of the test section but could also be a result of the lack of additional data points. From available data, approximately 60% of the test section provides steady in the Y-direction, in contrast with approximately 80% in the Z-direction.

The velocity data in Figs. 3.4 and 3.5 are used to obtain the boundary layer thickness at both ends of the Y- and Z-axes. The end of the boundary layer was determined to be the point where the normalized flow speed is 0.99 [50]. The exact location is determined from interpolation of available data. Boundary layer thickness is then plotted against the flow speed. Considering that the length of the test section in the Y- and Z-directions is 30.48 cm, the development of the boundary layer can be viewed from the $\frac{\mathrm{U}}{\mathrm{U_c}}$ plots of Figs. 3.4 and 3.5 respectively. Flow speeds of 0.92 and 1.97 m/s show a total boundary layer thickness of

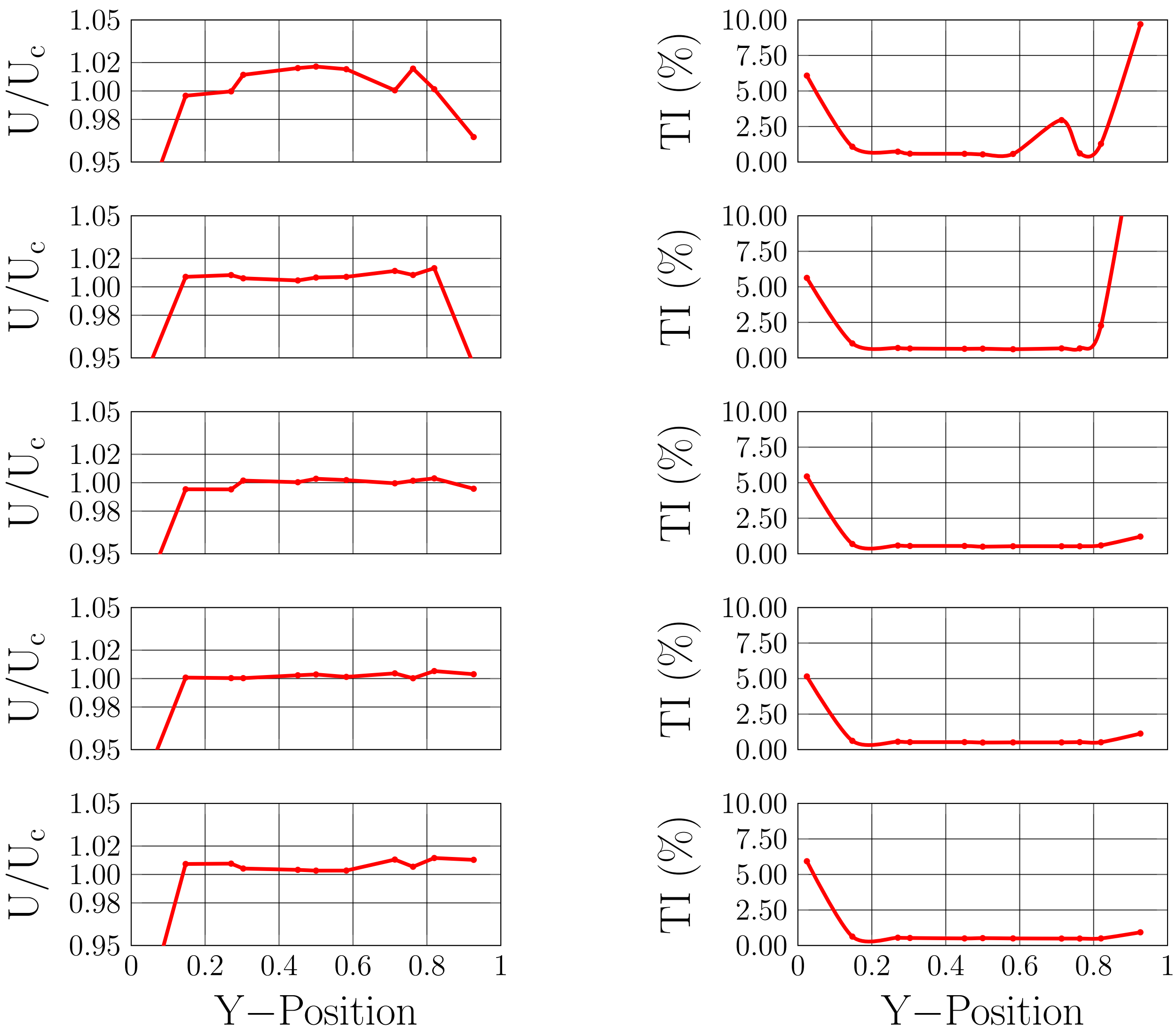

Figure 3.5: U/U$_c$ vs. y−position at 1, 2, 5, 8, & 10 m/s respectively (left) and turbulence intensity vs. y−position at 1, 2, 5, 8, & 10 m/s respectively (right)

38.7 mm on average, which corresponds to approximately 12.69% of the total test section length in the Z-axis. Flow speeds of 5.10, 8.00, and 10.12 m/s show a total boundary layer thickness of 27.9 mm, which corresponds to approximately 9.17% of the total test section length in the Z-axis. The limited data available for the Y-axis shows that the boundary layer at the top of the test section is larger than that of the bottom. At flow speeds of 5.10, 8.00, and 10.12 m/s, there is approximately a 20 mm difference in boundary layer thickness. The boundary layer thickness at the bottom of Y-axis follows a similar trend to that at the back

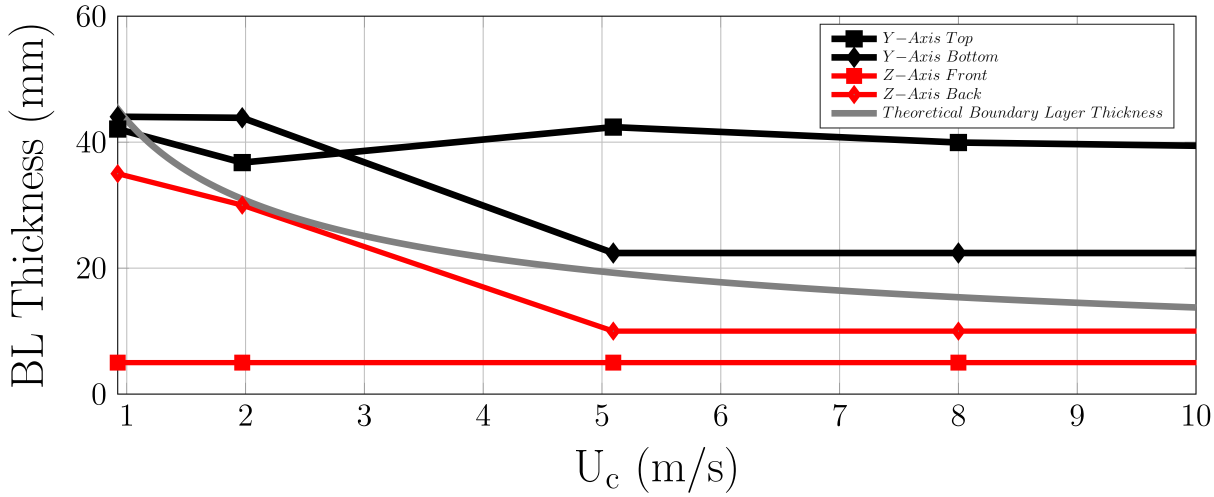

Figure 3.6: Y- and Z-axis boundary layer thickness

of the Z-axis, with approximately a 10 mm increase in thickness. Boundary layer thicknesses at the bottom of the Y-axis for 5.10, 8.00, and 10.12 m/s were recorded at the final data point obtained from the Y-axis because the normalized flow speed at these flow speeds did not fall below 0.99. In general, the boundary layer thickness did not exceed 45 mm, which corresponds to approximately 14.76% of the total test section length; this means that at any flow speed, the total boundary layer thickness will not exceed approximately 30% of the test section length or width. The theoretical boundary layer thickness is also plotted in Fig. 3.6. The boundary layer thickness was determined using [50],

$$\delta \sim \sqrt{\left(\frac{\nu x}{U_\infty}\right)}. \tag{3.1}$$

The beginning of the boundary layer was modeled as the exit of the contraction cone, making the distance, x, from the beginning of the boundary layer to the center of the test section approximately 2.13 m.

Fig. 3.7 displays the flow speed and turbulence intensity across the X-axis of the test section. The X-axis extends to approximately 65% of the total test section length due to the limitations discussed previously regarding the length of the traverse and time constraints.

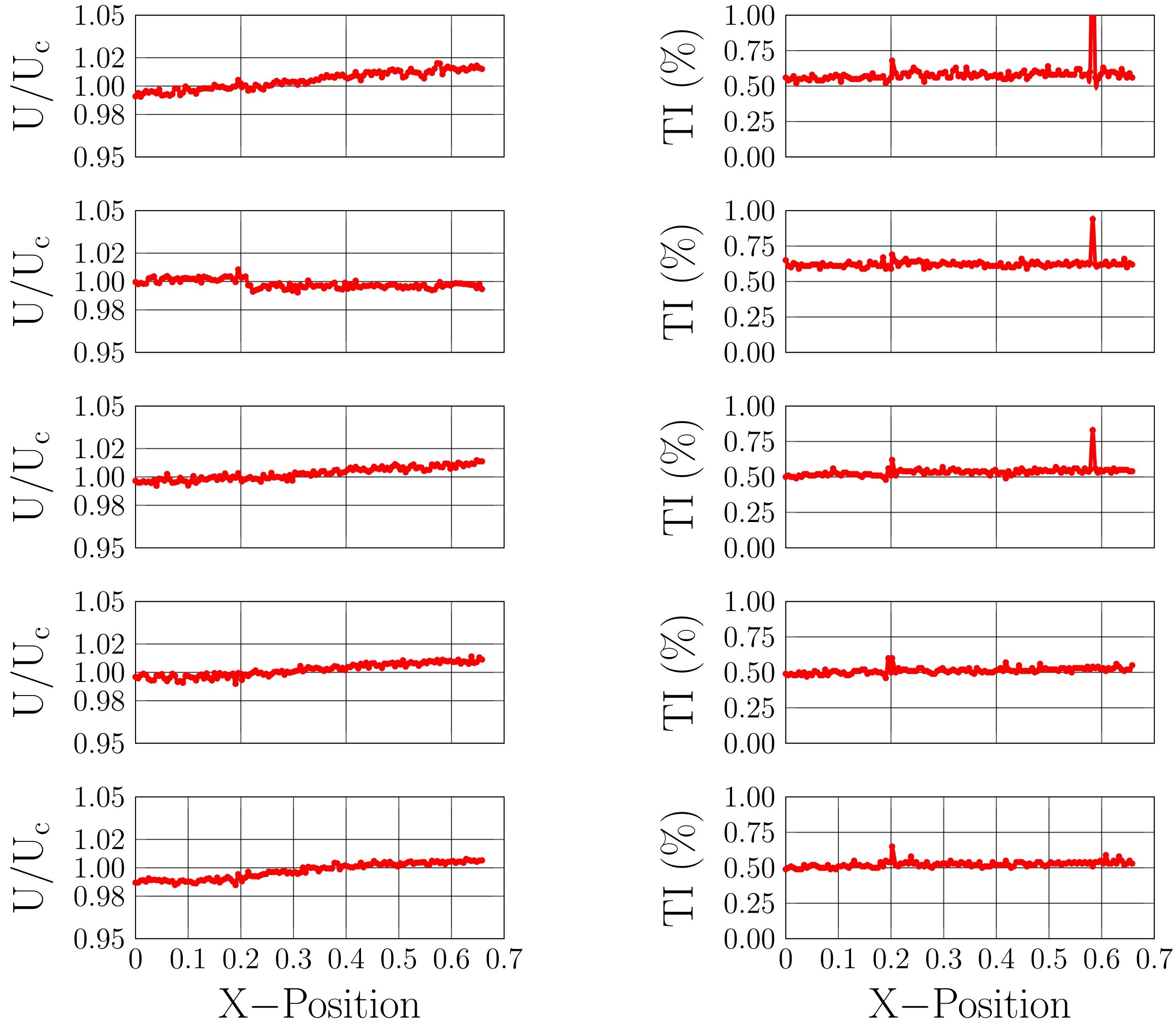

Figure 3.7: U/U_c vs. x−position at 1, 2, 5, 8, & 10 m/s respectively (left) and turbulence intensity vs. x−position at 1, 2, 5, 8, & 10 m/s respectively (right)

The turbulence intensity of each flow speed remains relatively constant and low, with a nominal value of approximately 0.60% for 0.92 and 1.97 m/s and 0.50% for 5.10, 8.00, and 10.12 m/s. While the turbulence intensity remains fairly constant, the flow speed within the test section accelerates slightly as fluid flows down the length of the test section; this is because as water flows down the length of the test section, the size of the boundary layer increases, resulting in a smaller cross-sectional area for free flowing fluid. The mass flow of fluid within the test section remains the same, requiring the flow to accelerate slightly to accommodate the decreased cross-sectional area. This feature is shown in the plots for each flow speed, with 1.97 m/s being the exception. The flow acceleration is fairly minor and flow speeds do not deviate greatly from the expected values. The turbulence intensity plots, specifically at 1, 2, and 5 m/s, show a spike at X-position of approximately 0.58. Because the increase in value occurs at an isolated point, it is likely that it is a result of laser interference at that point within the test section window.

Fig. 3.8 shows a snapshot of flow and turbulence intensity within the test section. The subfigures in Fig. 3.8 provide a visual for observations made in Figs. 3.4 and 3.7 regarding flow speed and turbulence intensity. The planes show flow acceleration down the length of the test section. The uneven distribution of turbulence and boundary layer size on both sides of the test section can also be seen. Flow acceleration and turbulence fluctuation is more extreme at lower flow speeds (1 and 2 m/s). Turbulence intensity and flow speed fluctuations at the boundary layer have lower values at 5 m/s and the boundary layer is thinnest at 8 and 10 m/s. The color map for flow speed has been normalized to unity for each velocity measurement, while the turbulence planes show turbulence intensity percentage. Limitations with the laser doppler anemometry system prevented the collection of data at the top and bottom of the test section, as well as in small sections near the edge of the test section. As a result, the boundary layer in these areas is not shown in Fig. 3.8.

Fig. 3.9 displays flow planes for velocity and turbulence intensity. Each plane represents a snapshot of the test section at X = 0. Fig. 3.9 compares flow behavior at the center of the test section across various flow speeds. The velocity planes show accelerated flow for 1 and 2 m/s, while 5, 8, and 10 m/s show flow approximately at unity when compared to the colorbar. The turbulence intensity planes show an average value of approximately 0.5% outside of the boundary layer. Both sets of images in Fig. 3.9 show a decrease in boundary layer size as flow speed increases. The white spaces in Fig. 3.9 are missing data points due to laser limitations.

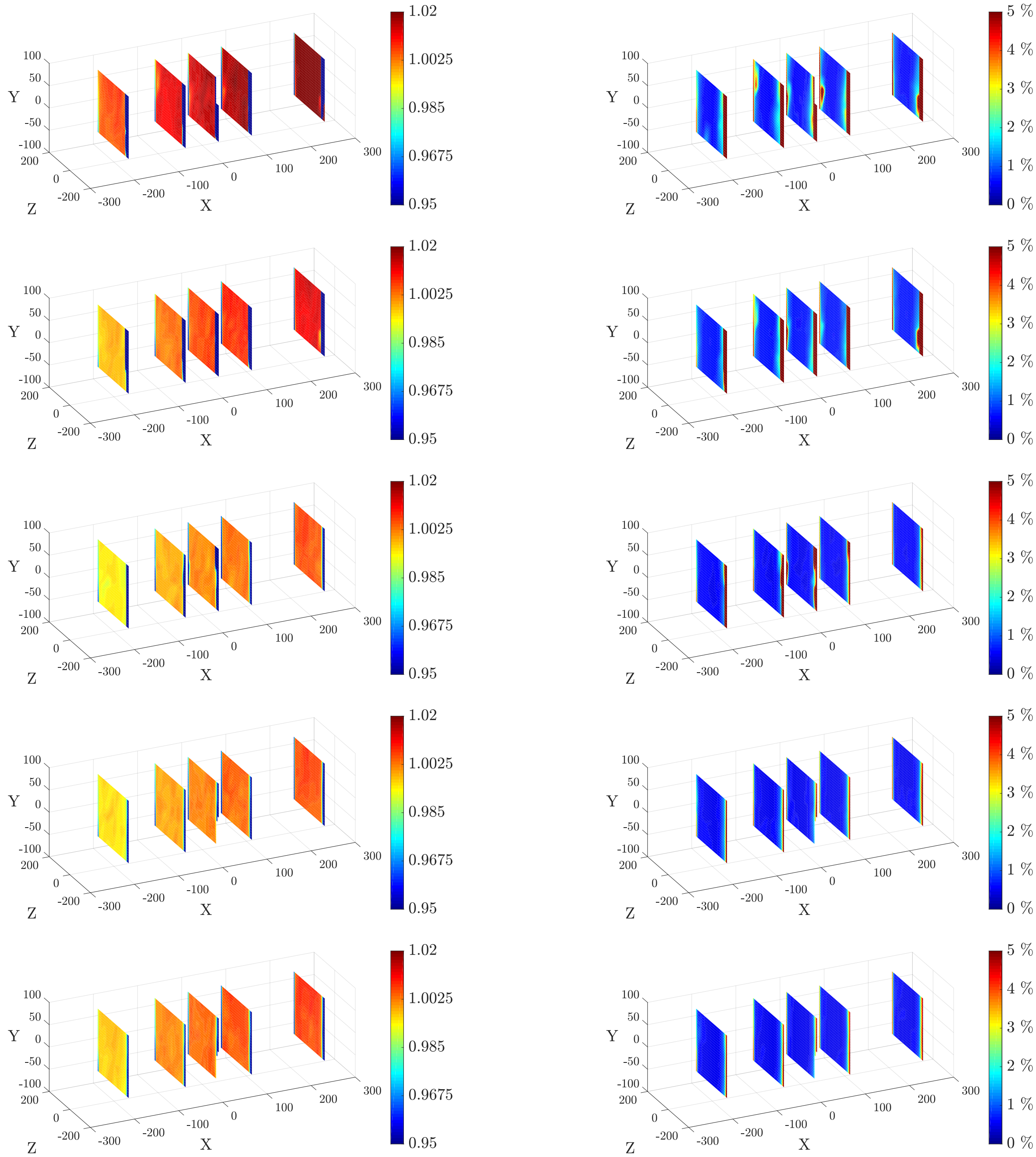

Figure 3.8: Left: Flow planes show velocity in the test section at 1, 2, 5, 8, and 10 m/s respectively. Right: Flow planes show turbulence intensity in the test section at 1, 2, 5, 8, and 10 m/s respectively.

The Fast Fourier Transforms (FFTs) in Fig. 3.10 display the frequency content of the test section flow. In this case, the FFTs convert data from the time domain to the frequency domain. The FFTs are taken for flow at the center of the test section at 1, 2, 5, 8, and 10 m/s. The absence of peak frequencies and downward sloping nature of the FFTs in Fig. 3.10 show that the water tunnel does not display excited frequency content for the flow speeds being reviewed. The data for each flow speed in Fig. 3.10 were collected at different sampling rates. As a result, each FFT is plotted to a different frequency—the Nyquist frequency of the data set—to avoid aliasing, an effect that occurs when signals become misidentified because it is measured at an insufficient sampling rate [51]. The Nyquist frequency is equivalent to half the sampling rate of each data set. The FFTs are plotted against a $f^{-5/3}$ roll off curve, as described in [52].

The results from the qualification data speak to the quality of the water tunnel. Small boundary layers mean that viscous forces are negligible for the bulk of the flow region within the test section [50]. The boundary layer at the walls of the test section can be easily avoided unless otherwise required for an experiment. Outside of the boundary layer, it can be seen in Fig. 3.8 that the velocity profiles and turbulence intensities across various flow speeds are consistent; the test section does experience flow acceleration down the length of the test section however. Turbulence intensity values are small outside of the boundary layer, with an average value around 0.5%. The distribution of flow speeds and turbulence intensities across the test section show that experiments conducted in the water tunnel, specifically towards the center of the test section, will be subject to a uniform velocity profile and low turbulence. It has also been shown that the tunnel can consistently reach expected flow speeds when driven at specified motor frequencies. The tunnel easily has the ability to operate at up to 10 m/s for extended periods of time, and has shown potential to flow at speeds greater than 10 m/s. It is expected that by increasing both the tension within the motor belts and the pressure within the tunnel, higher flow speeds will be attained while reducing the potential for cavitation in the test section.

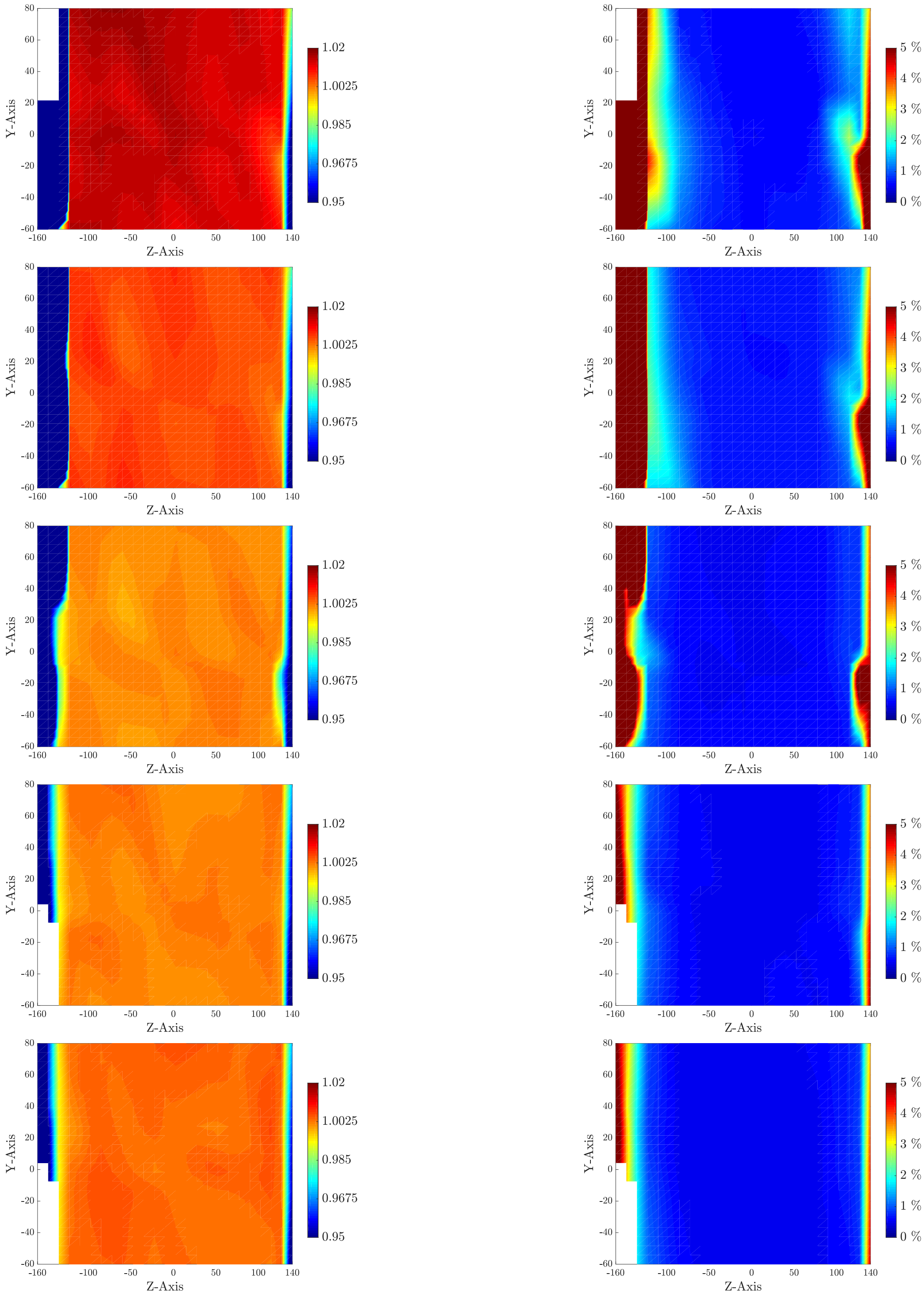

Figure 3.9: Left: Flow planes show the velocity distribution at X = 0 across 1, 2, 5, 8, and 10 m/s respectively. Bottom: Flow planes show the turbulence intensity at X = 0 across 1, 2, 5, 8, and 10 m/s respectively.

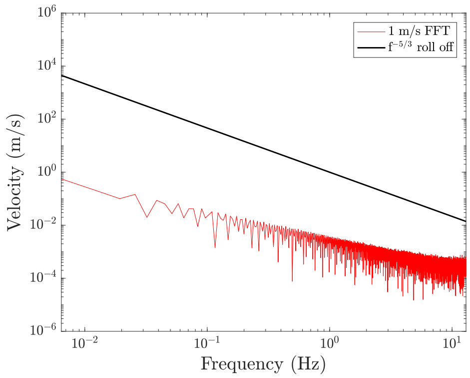

(a)

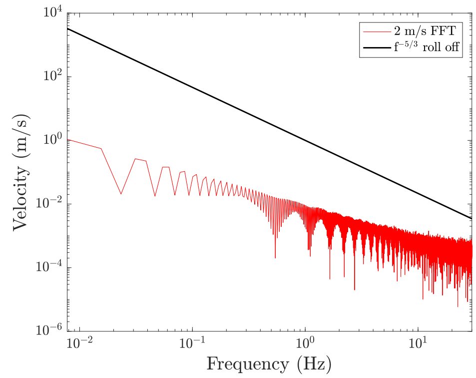

(b)

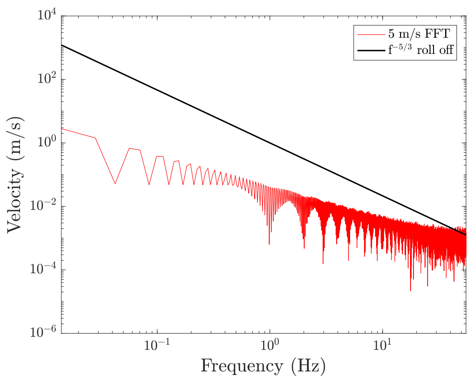

(c)

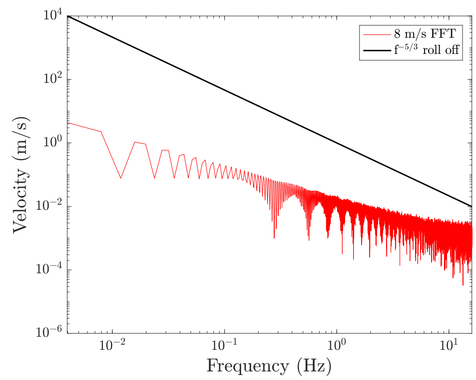

(d)

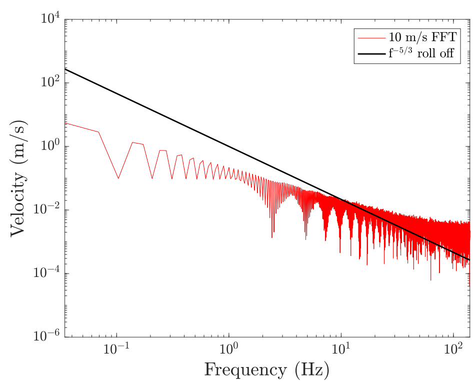

(e)

Figure 3.10: Fast Fourier Transforms (FFTs) of velocity data at test section center; subfigures (a), (b), (c), (d), (e) correspond to 1, 2, 5, 8, and 10 m/s respectively

Chapter 4

Conclusion

4.1 Summary

This thesis details the design and fabrication of the high-speed water tunnel at the University of Georgia. The tunnel, currently in operation, delivers uniform flow up to 10 m/s and is being used to conduct fluid-structure interaction experiments. The work describes the major components of the water tunnel and their functions. It also discusses the qualification procedure and results.

The test section, used to test models and collect data, is based on the redesign of the HiCaT. The desired size of the test section—a 1.00 m long, 30.48 cm square cross section—was specified during its initial design. Acrylic was selected as the window material for its excellent optical penetration. A steel flange was cut and placed around the window to evenly distribute bolt loads across the acrylic. The diffuser decelerates flow exiting the test section. A half angle of 3° was selected for the UGA tunnel diffuser. The half angle determined the length of the diffuser to be approximately 3.05 m. The contraction cone increases flow speed while minimizing the increase of turbulence in the test section. A fifth-order polynomial was used to form the shape of the contraction. The shape generated difficulties during fabrication, but an exoskeleton was created for the contraction and the walls were formed around the exoskeleton. A 93,213 W motor, along with a bronze propeller, was selected to drive the system based on calculations for required flow speeds. The propeller is connected to a sacrificial anode, zinc, which will corrode in lieu of the bronze.

The UGA tunnel was qualified using a LDA system. A grid of points was generated for the laser to create a map of the test section. The grid was used to collect data at 1, 2, 5, 8, and 10 m/s. The data establishes that the tunnel generates laminar up to 10 m/s while maintaining boundary layer thicknesses below 35 mm. The data also shows an average turbulence intensity value of of approximately 0.5% outside the boundary layer.

4.2 Lessons Learned

Many difficulties were faced during the design and qualification of the UGA water tunnel. To aid future efforts surrounding design and qualification, a list of lessons learned/suggestions has been created.

1. Mark the physical laser position when it is placed at center of test section, so that it can be consistently moved to the entrance and exit of the test section.
2. Reset the laser position at the center of the test section after each qualification run to ensure the consistency of the laser placement.
3. Make sure acrylic glass is as clean as possible before starting each run.
4. If dry erase marker used to mark on acrylic windows, LDA lasers can melt marker into acrylic.

5. Do not qualify with aluminum plate, or any reflective surface, attached to the test section.

6. Check and make sure software settings are consistent for every qualification run.

7. Maintain sterile environment inside tunnel to avoid build up for hot wire use. Debris inside the tunnel can affect hot wire measurements and lead to damage of the hot wire probe.

Chapter 5

Bibliography

[1] D. Simms, S. Schreck, M. Hand, and L. J. Fingersh, "NREL unsteady aerodynamics experiment in the NASA-Ames wind tunnel: A comparison of predictions to measurements," Tech. Rep. NREL/TP-500-29494, NASA, June 2001.

[2] W. J. McCroskey, "A critical assessment of wind tunnel results for the NACA 0012 airfoil," Tech. Rep. 87-A-5, NASA, Oct. 1987.

[3] R. Luidens and P. Simon, "Aerodynamic characteristics of NACA RM-10 missile in 8- by 6-foot supersonic wind tunnel at Mach numbers from 1.49 to 1.98," Tech. Rep. NACA-RM-E50D28, NASA, July 1950.

[4] S. Ristic, "A-A view in the invisible," *Theoretical and Applied Mechanics*, vol. 40, no. 1, pp. 87–119, 2013.

[5] W.-H. Chu, "A critical re-evaluation of hydrodynamic theories and experiments in subcavitating hydrofoil flutter," *Journal of Ship Research*, June 1966.

[6] L. G. Straub, J. F. Ripken, and R. M. Olson, "The six-inch water tunnel at the St. Anthony Falls Hydraulic Laboratory and its experimental use in cavitation design stud-

ies," Tech. Rep. 16, University of Minnesota; St. Anthony Falls Hydraulic Laboratory, Sept. 1955.

[7] I. Nedyalkov, "Design of contraction, test section, and diffuser fro a high-speed water tunnel," Master's thesis, Chalmers University of Technology, 2012.

[8] L. Daniel, "Design and installation of a high reynolds number recirculating water tunnel," Master's thesis, Embry-Riddle Aeronautical University, 2012.

[9] S. Hu, C. Lu, and Y. He, "Fluid-structure interaction simulation of three-dimensional flexible hydrofoil in water tunnel," *Applied Mathematics and Mechanics*, vol. 37, pp. 15–26, Dec. 2015.

[10] J. W. Daily, "The water tunnel as a tool in hydraulic research," in *Proceedings of the Third Hydraulics Conference*, California Institute of Technology, 1947.

[11] Y. Young, "Fluid–structure interaction analysis of flexible composite marine propellers," *Journal of Fluids and Structures*, vol. 24, pp. 799–818, Aug. 2008.

[12] R. Etter and M. Wilson, "The large cavitation channel," in *Proceedings of the 23rd American Towing Tank Conference*, pp. 243–252, 1992.

[13] M. Wosnik and R. Arndt, "Testing of a 1:6 scale physical model of the large, low-noise cavitation tunnel (locat)," 2006.

[14] R. Sato, T. Mori, R. Yakushiji, K. Naganuma, M. Nishimura, K. Nakagawa, and T. Sasajima, "Conceptual design of the flow noise simulator," in *ASME/JSME 2003 4th Joint Fluids Summer Engineering Conference*, pp. 129–133, American Society of Mechanical Engineers, 2003.

[15] E. Weitendorf and H. Tanger, "Cavitation correlation and nuclei investigations in two water tunnels-comparisons in the hykat and the medium size tunnel," *Proceedings of the Institution of Mechanical Engineers*, p. C453, 1992.

[16] J. Wetzel and R. Arndt, "Hydrodynamic design considerations for hydroacoustic facilities: part iflow quality," *Journal of fluids engineering*, vol. 116, no. 2, pp. 324–331, 1994.

[17] P. Brandner, Y. Lecoffre, and G. Walker, "Design considerations in the development of a modern cavitation tunnel," 2007.

[18] E.-A. Weitendorf, "Cavitation phenomena, propeller excited hull pressure amplitudes and cavitation scale effect," *Ocean Engineering*, vol. 8, no. 5, pp. 517–539, 1981.

[19] L. Daniel, *Design and installation of a high Reynolds number recirculating water tunnel.* Oklahoma State University, 2014.

[20] A. Fontaine, J. Crafton, S. Fonov, E. Jones, and L. Goss, "Evaluation of the ISSI S3F film for distributed measurements of pressure gradient and wall-shear in water at high Reynolds number," tech. rep., Pennsylvania State University Park Applied Reserach Lab, 2006.

[21] L. Daniel, S. Mohagheghian, D. Dunlap, E. Ruhlmann, and B. R. Elbin, "Design of a recirculating water tunnel for the study of high-reynolds number turbulent boundary layers," in *ASME 2015 International Mechanical Engineering Congress and Exposition*, ASME, 2015.

[22] R. Arndt, V. Arakeri, and H. Higuchi, "Some observations of tip-vortex cavitation," *Journal of fluid mechanics*, vol. 229, pp. 269–289, 1991.

[23] J.-B. Leroux, J. A. Astolfi, and J. Y. Billard, "An experimental study of unsteady partial cavitation," *Journal of fluids engineering*, vol. 126, no. 1, pp. 94–101, 2004.

[24] A. F. Lehman, *The Garfield Thomas Water Tunnel.* Ordnance Research Laboratory, 1959.

[25] W. Brownell, “A 36-inch variable pressure water tunnel,” *David Taylor Model Basin Report*, vol. 1052, 1956.

[26] G.-H. Choi, B.-J. Chang, and D.-S. Cho, “Cavitation test at high reynolds number using a partial propeller blade model,” *Journal of the Society of Naval Architects of Korea*, vol. 46.

[27] W. lJ Brownell, “Preijiminary hxdraulic design studies for alterations to the 24-inch variable-pressure water tunnel,” *Navy Department, David Taylor Model Basin*, 1948.

[28] N. Madavan, S. Deutsch, and C. Merkle, “Reduction of turbulent skin friction by microbubbles,” *The Physics of Fluids*, vol. 27, no. 2, pp. 356–363, 1984.

[29] S. Deutsch and J. Castano, “Microbubble skin friction reduction on an axisymmetric body,” *The Physics of fluids*, vol. 29, no. 11, pp. 3590–3597, 1986.

[30] G. F. Oweis, J. Choi, and S. L. Ceccio, “Dynamics and noise emission of laser induced cavitation bubbles in a vortical flow field,” *The Journal of the Acoustical Society of America*, vol. 115, no. 3, pp. 1049–1058, 2004.

[31] E. O. Hansen, “Qualitative and quantitative determination of the flow around a cavitating flat plate perpendicular to the flow in a two-dimensional test section,” *David Taylor Model Basin, Washington, D. C in ASME*, pp. 6–8, 1967.

[32] K. Kaku, “The design of a small water tunnel and its use in evaluating surface roughness effects on cavitation,” , vol. 13, no. 3, pp. 527–584, 1965.

[33] D. Weir, M. Billet, and J. Holl, “The 1.5-inch ultra-high-speed cavitation tunnel at the applied research laboratory of the Pennsylvania State University.,” tech. rep., Pennsylvania State University Park Applied Research Lab, 1975.

[34] S. C. Ko, “Design and construction of a water tunnel,” Jan. 1971.

[35] R. Robinson, D. Butterfield, D. Curtis, and T. Thompson, "Problems with Pitots issues with flow measurement in stacks," *International Environmental Technology (IET)*, 2004.

[36] R. Klopfenstein, "Air velocity and flow measurement using a Pitot tube," *ISA Transactions*, vol. 37, pp. 257–263, Sept. 1998.

[37] G. Comte-Bellot, "Hot-wire anemometry," *Annual Review of Fluid Mechanics*, vol. 8, pp. 209–231, Jan. 1976.

[38] N. Nouri, K. Mostafapour, M. Kamran, and R. Bohadori, "Design methodology of a six-component balance for measuring forces and moments in water tunnel tests," *Measurement*, vol. 58, pp. 544–555, Dec. 2014.

[39] H. Werle, "Hydrodynamic flow visualization," *Annual Review of Fluid Mechanics*, vol. 5, pp. 361–386, Jan. 1973.

[40] A. J. Smits and T. T. Lim, *Flow Visualization: Techniques and Examples*. Imperial College PR, second ed., Sept. 2012.

[41] J. B. Barlow, J. W. H. Rae, and A. Pope, *Low-Speed Wind Tunnel Testing*. John Wiley & Sons, Inc., third ed., 1999.

[42] G. Thomson, "The Antoine equation for vapor-pressure data.," *Chemical reviews*, vol. 38, no. 1, pp. 1–39, 1946.

[43] G. Batchelor, *An introduction to fluid dynamics*. Cambridge University Press, 2000.

[44] D. Ross, J. M. Robertson, and R. B. Power, "Hydrodynamic design of the 48-inch water tunnel at the Pennsvlvania State College," Tech. Rep., The Ordnance Research Laboratory of The Pennsylvania State College, Jan. 1948.

[45] V. Uruba, "Dynamics of flow behind backward-facing step in a narrow channel," *EPJ Web of Conferences*, vol. 45, p. 01108, 2013.

[46] J. Lumley and J. McMahon, "Reducing water turbulence by means of a honeycomb," *Journal of Basic Engineering*, vol. 89, no. 4, pp. 764–770, 1967.

[47] D. A. Johnson, "Laser Doppler anemometry," Tech. Rep. 1000072, NASA, June 1988.

[48] M. Puharic, S. Ristic, M. Kutin, and Z. Adamovic, "Laser Doppler anemometry in hydrodynamic testing," *Journal of Russian Laser Research*, vol. 28, pp. 619–628, Nov. 2007.

[49] W. Haynes, "Students t-test," in *Encyclopedia of Systems Biology*, pp. 2023–2025, Springer, 2013.

[50] H. Schlichting and K. Gersten, *Boundary-Layer Theory*. Springer-Verlag Berlin Heidelberg, 9th ed., 2017.

[51] M. Raffel, C. Willert, S. Wereley, and J. Kompenhans, *Particle Image Velocimetry*. Springer-Verlag GmbH, second ed., 2007.

[52] C. Foias, D. D. Holm, and E. S. Titi, "The navier–stokes-alpha model of fluid turbulence," *Physica D: Nonlinear Phenomena*, vol. 152, pp. 505–519, Mar. 2001.

Appendices

Appendix A

UGA Water Tunnel Sketch

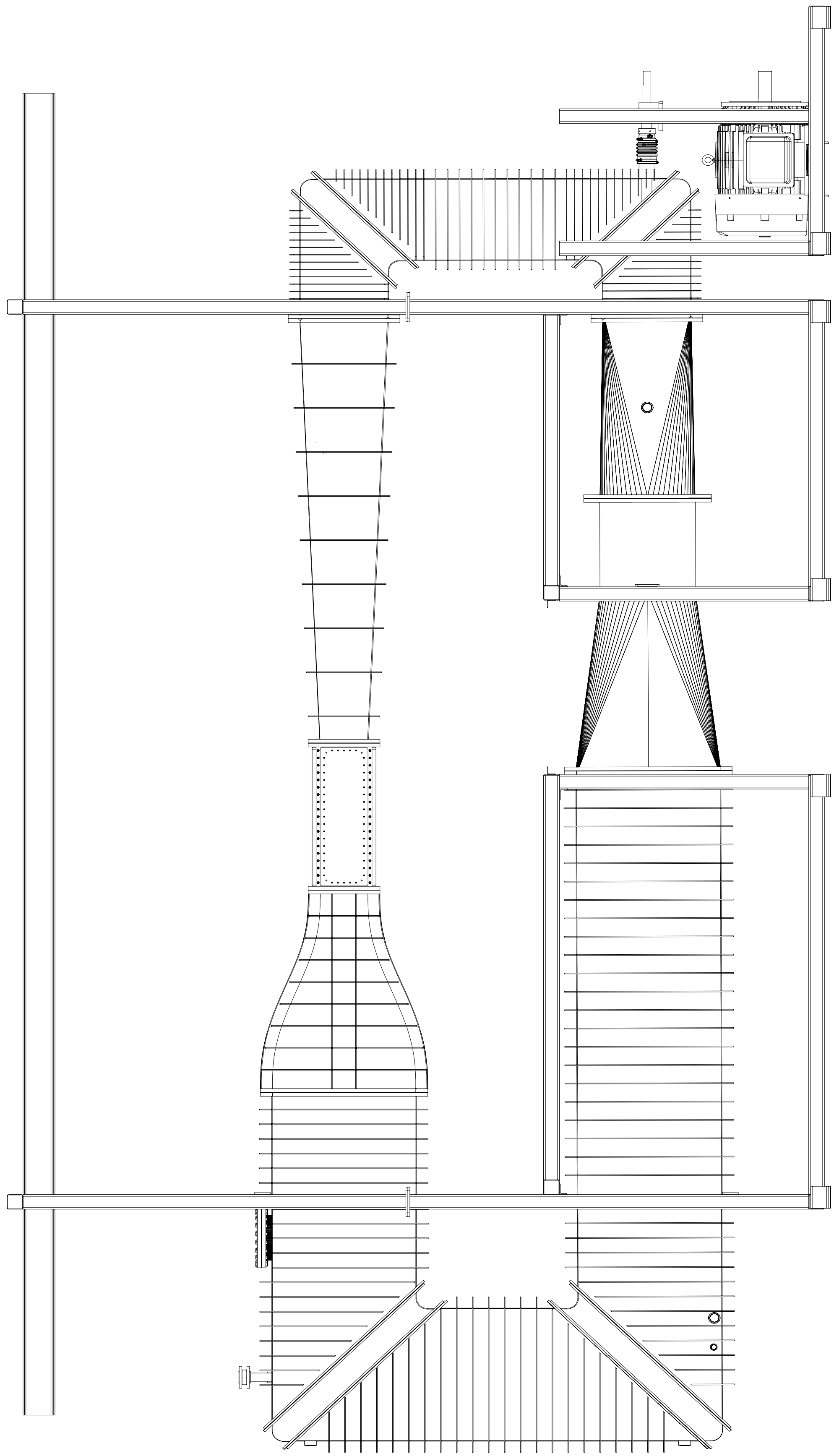

Figure A.1: UGA water tunnel sketch side profile

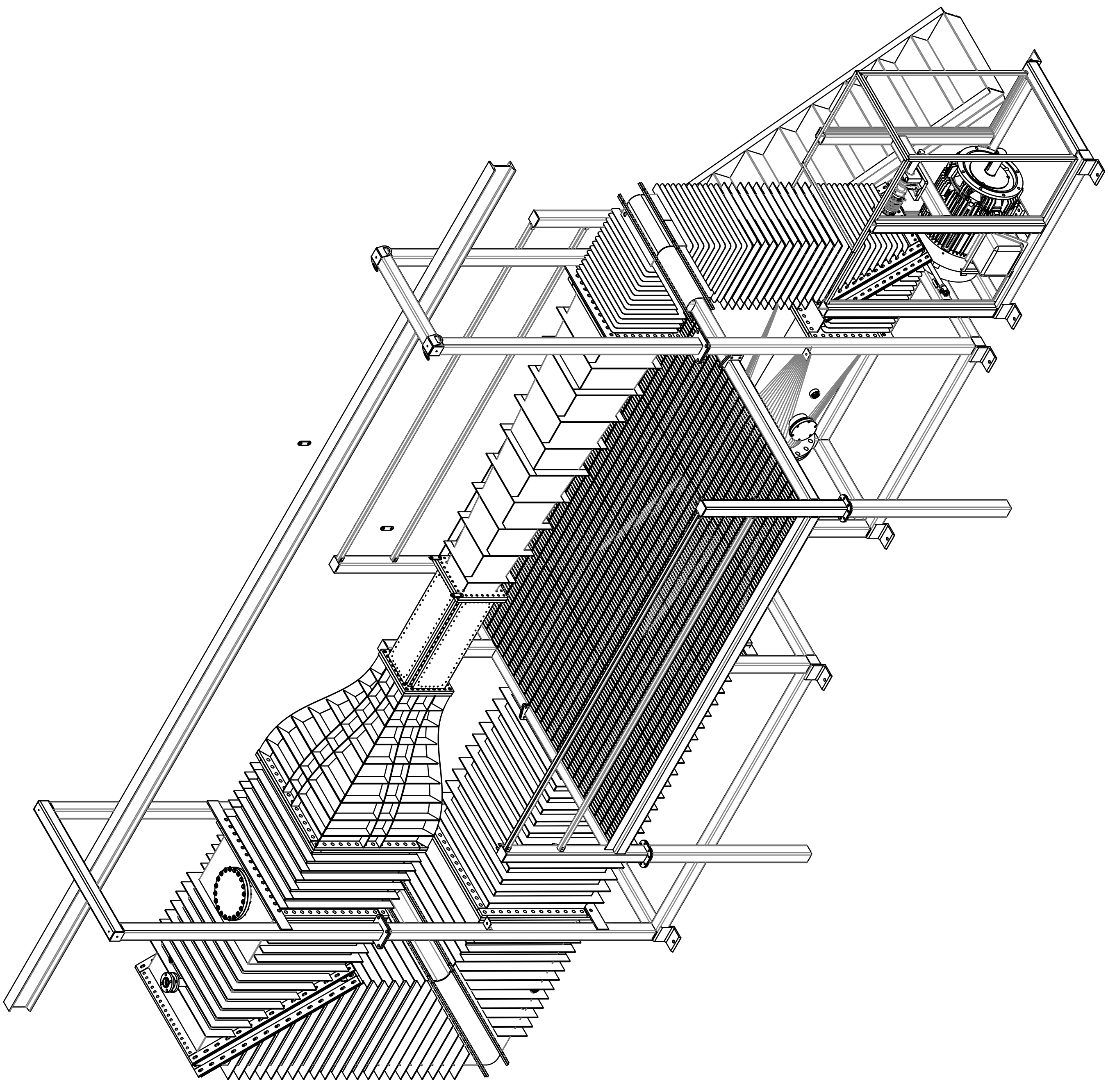

Figure A.2: UGA water tunnel sketch isometric profile

Appendix B

UGA Water Tunnel Component Drawings

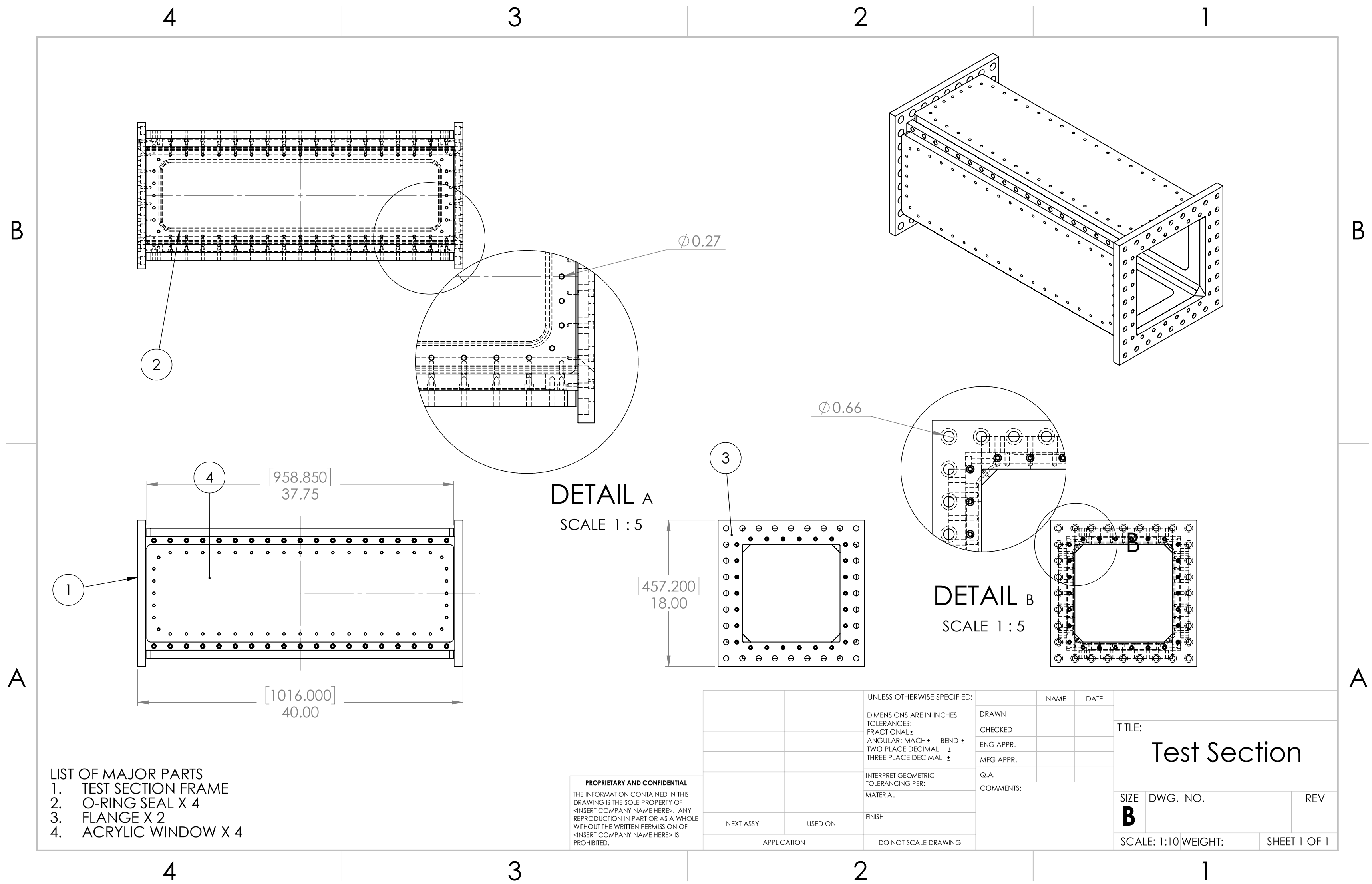

Figure B.1: Test section assembly drawing

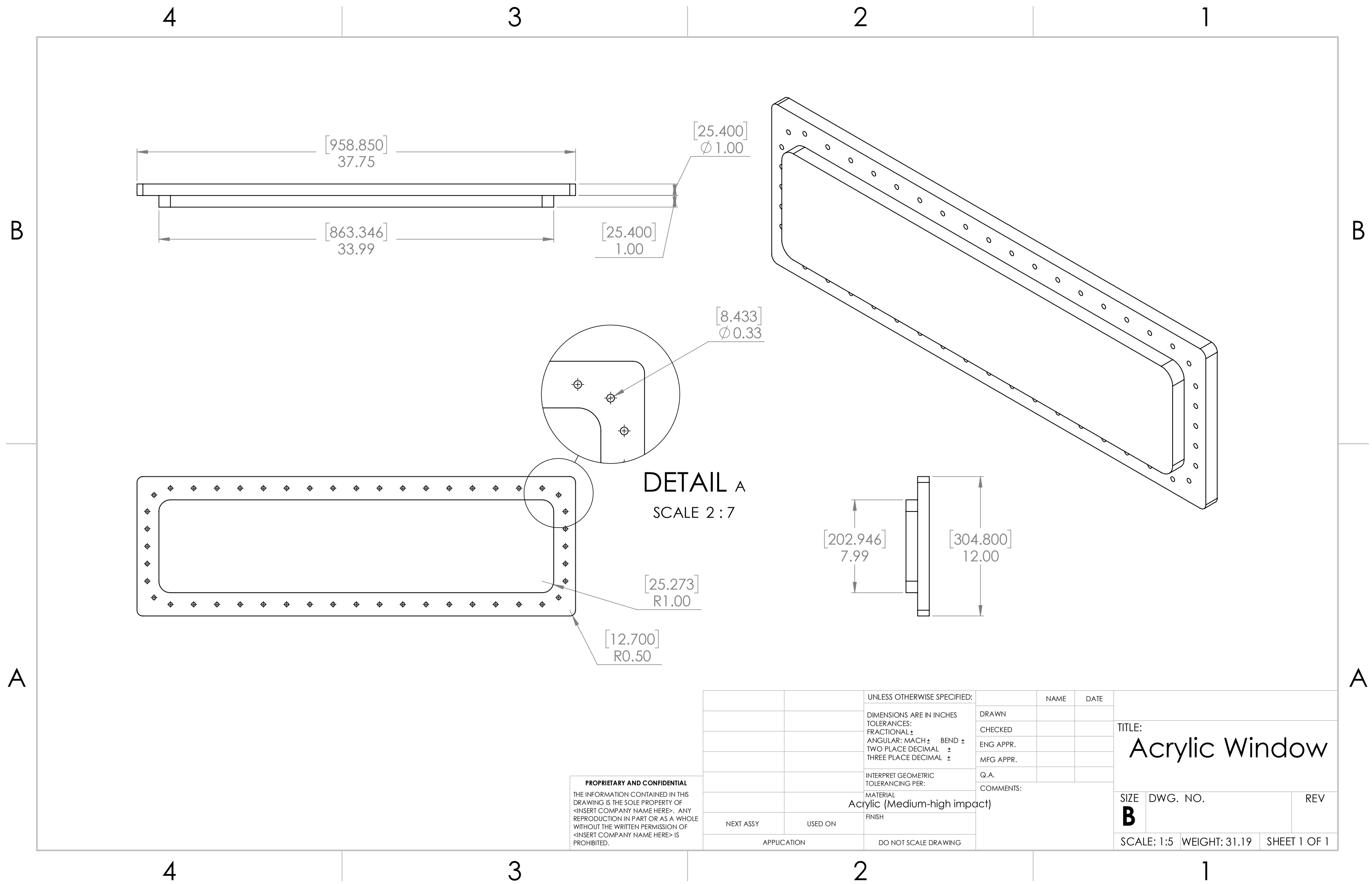

Figure B.2: Test section acrylic window drawing

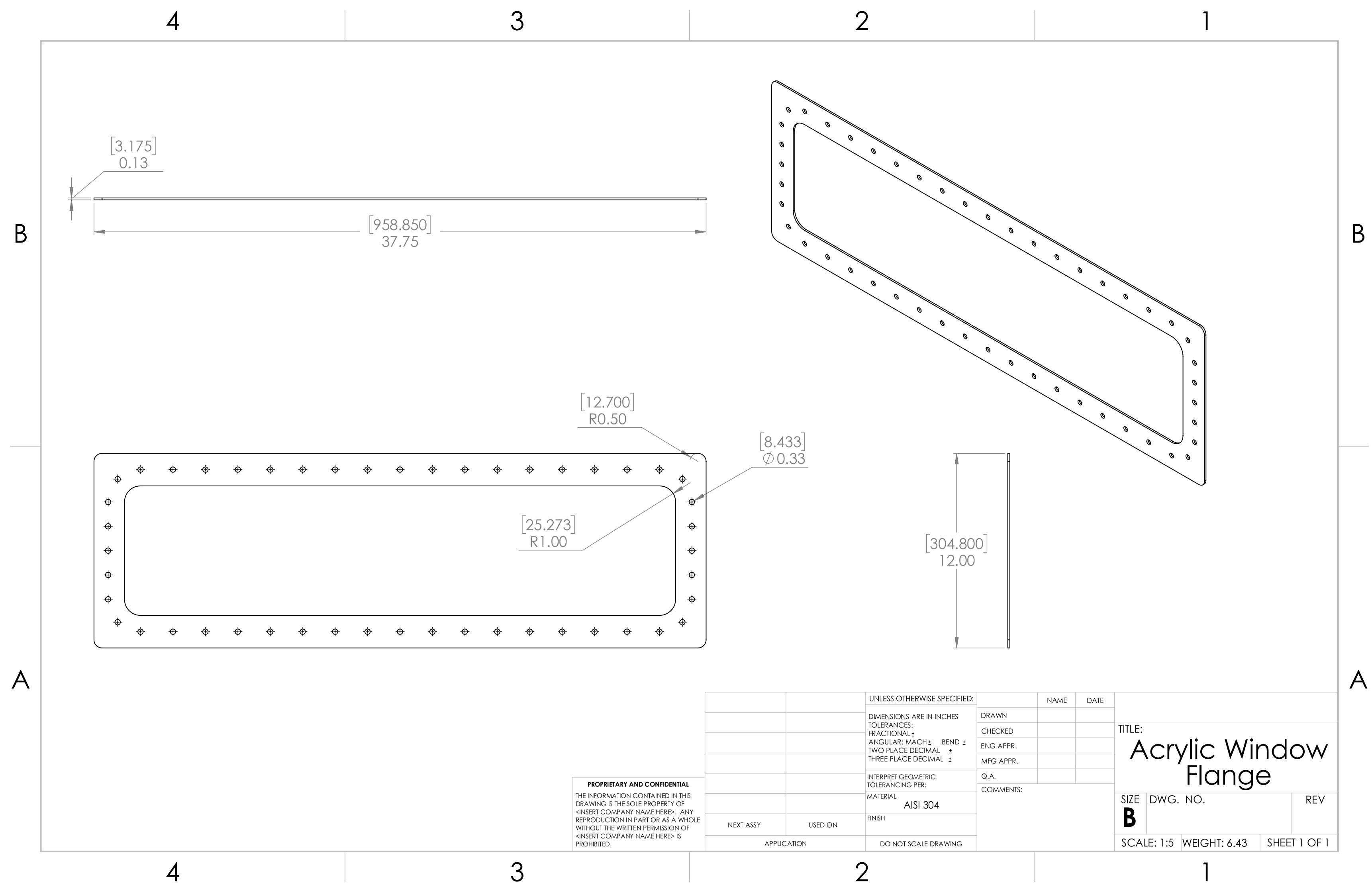

Figure B.3: Test section acrylic window flange drawing

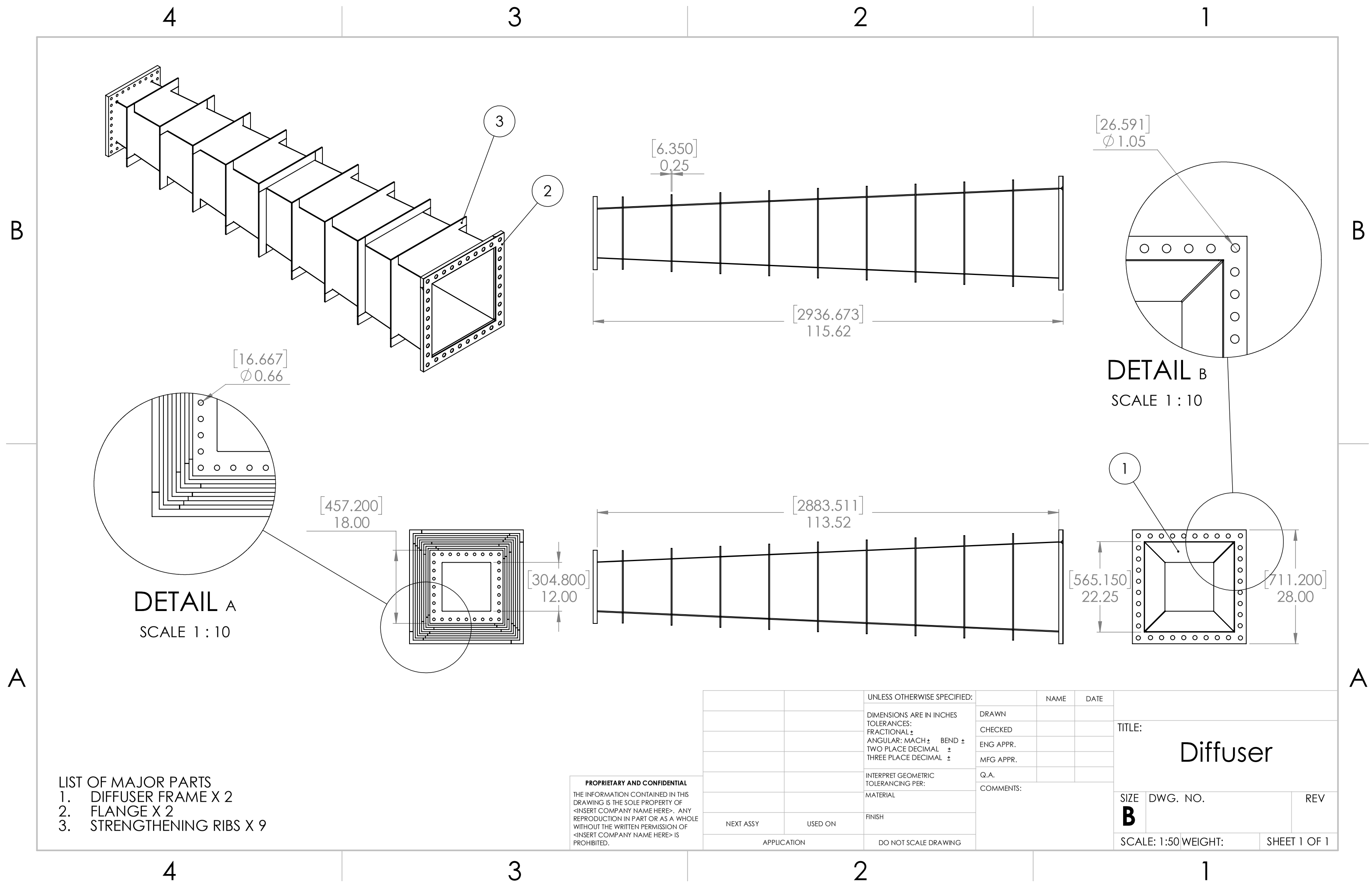

Figure B.4: Diffuser drawing

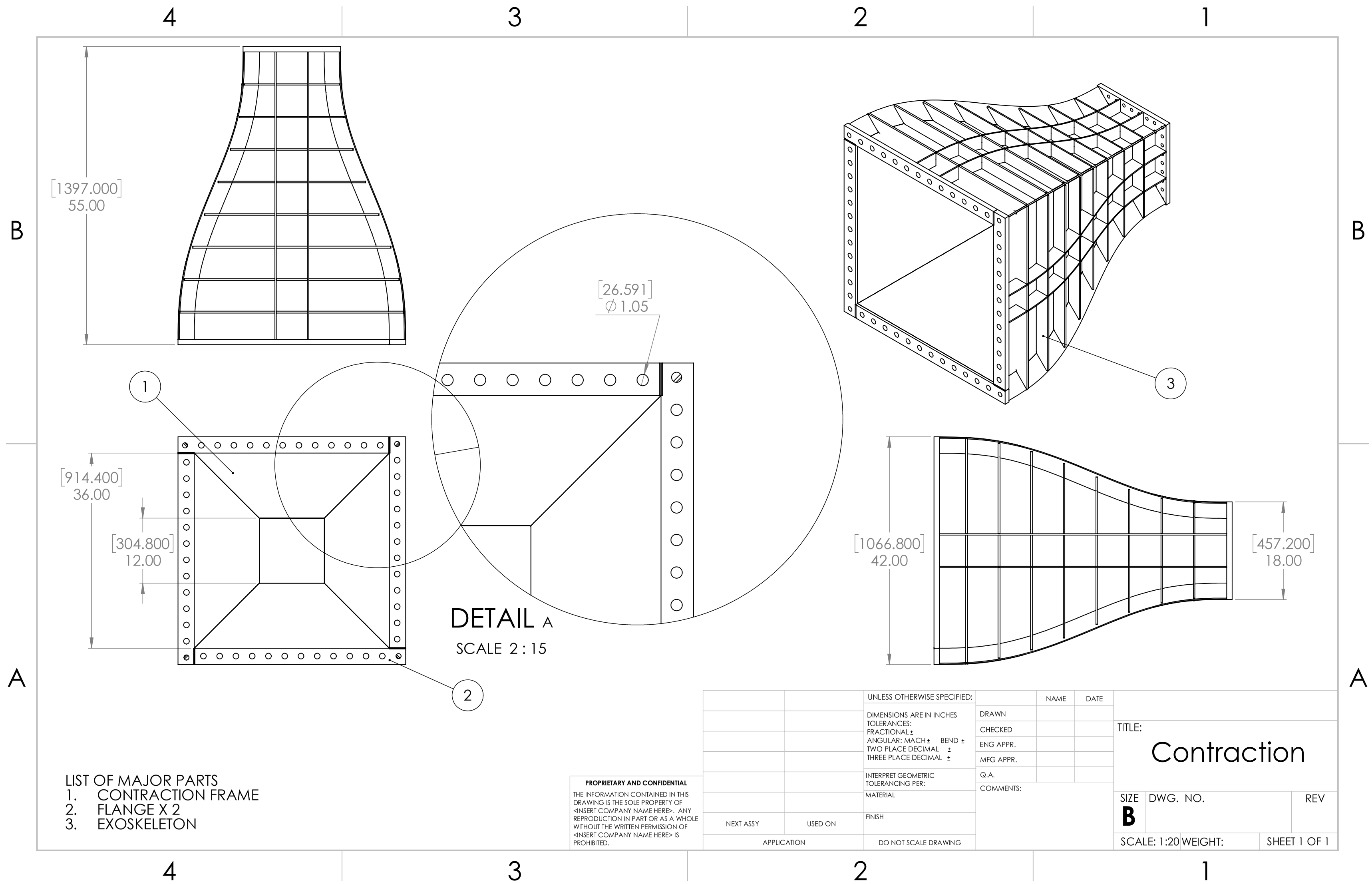

Figure B.5: Contraction cone drawing

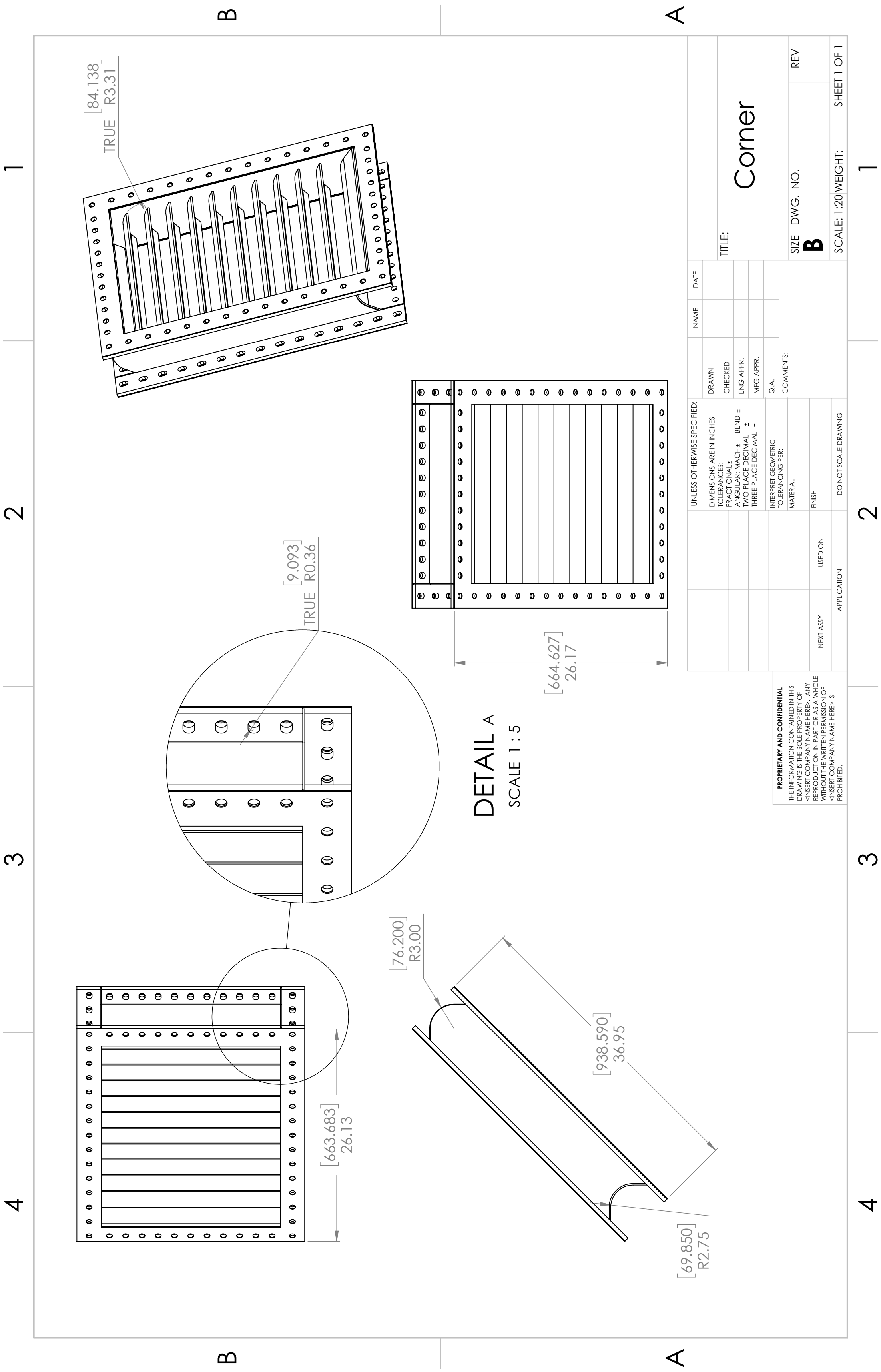

Figure B.6: Turning vanes drawing

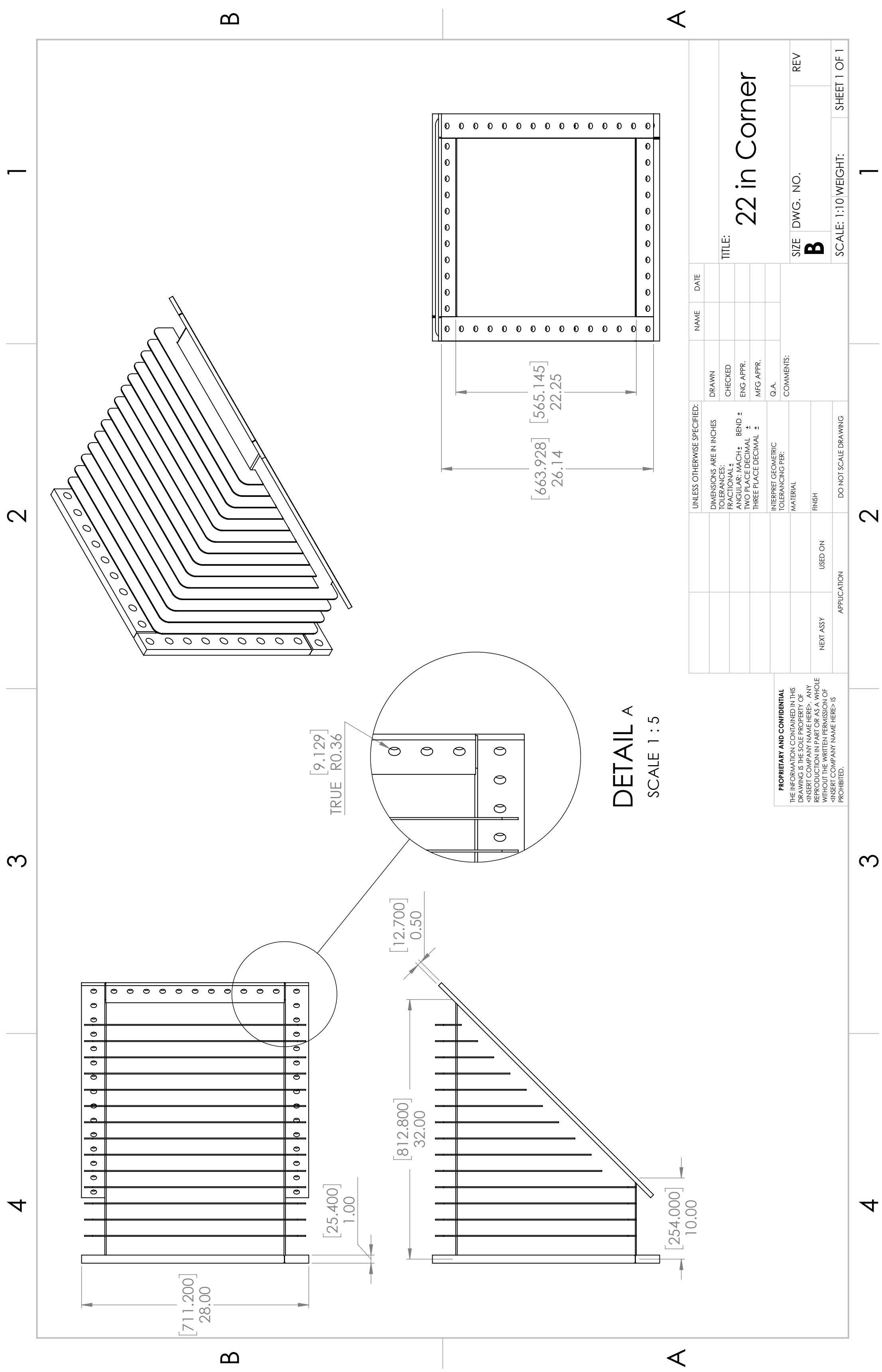

Figure B.7: Corner drawing.

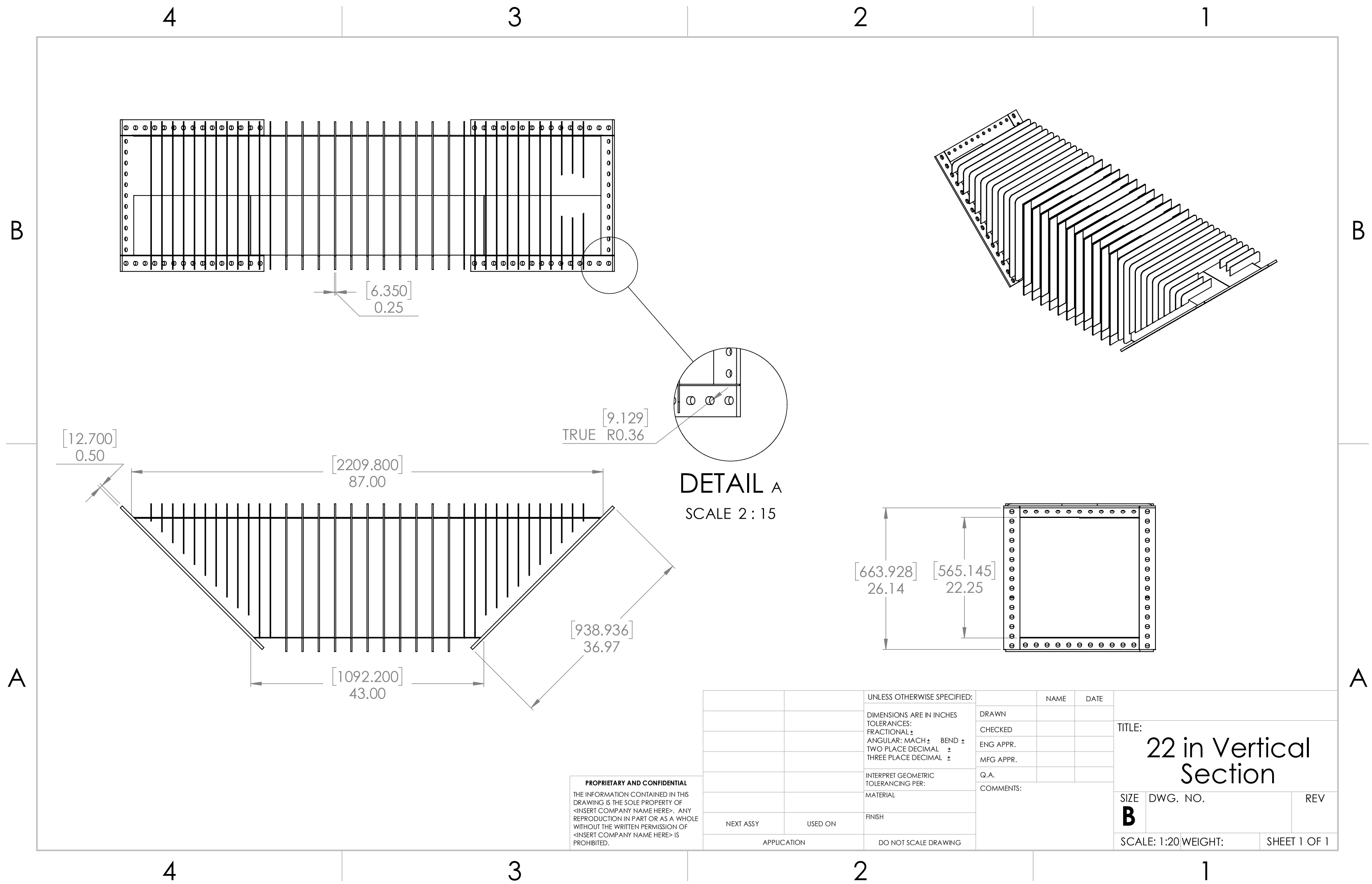

Figure B.8: Vertical section drawing

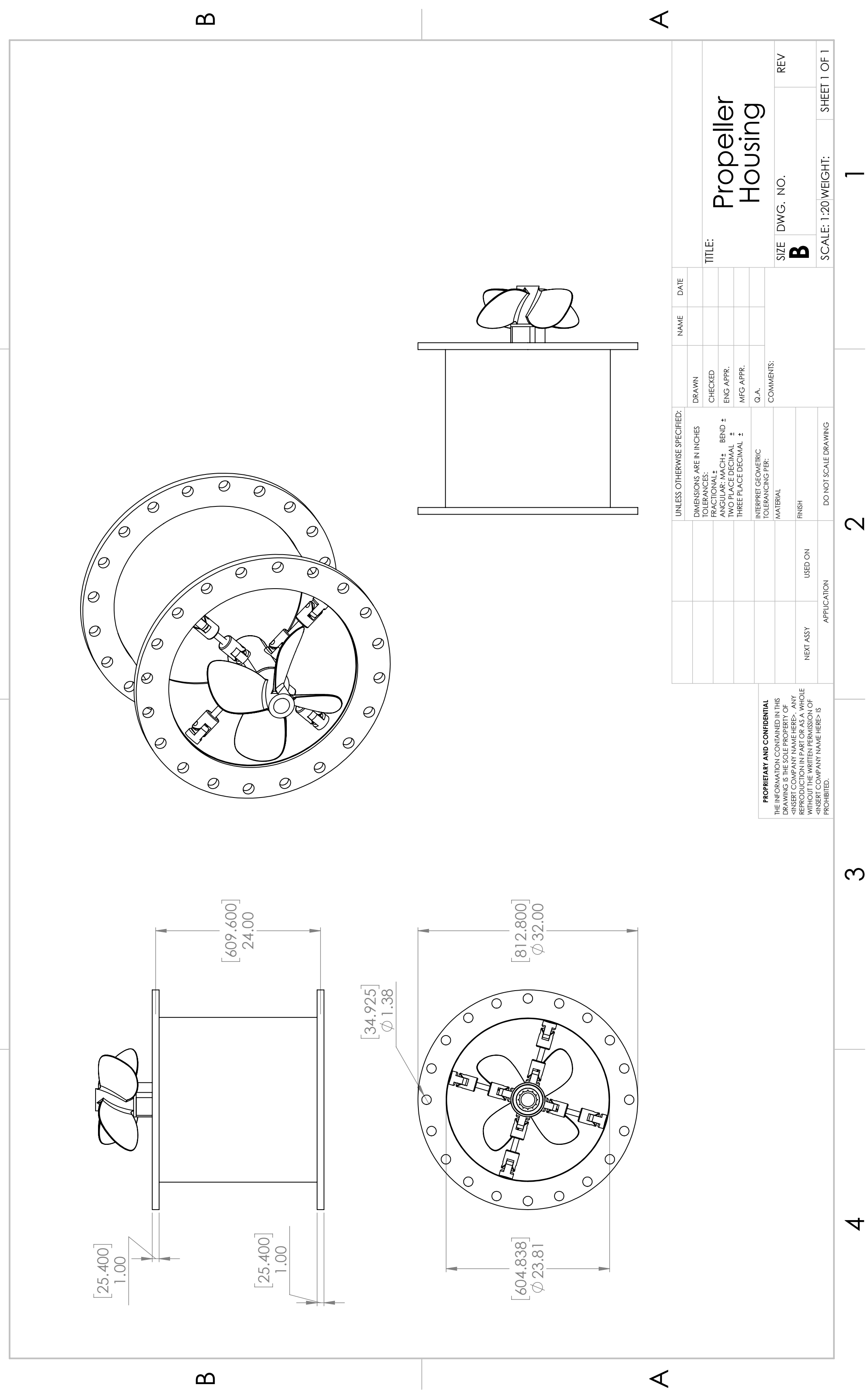

Figure B.9: Propeller housing drawing

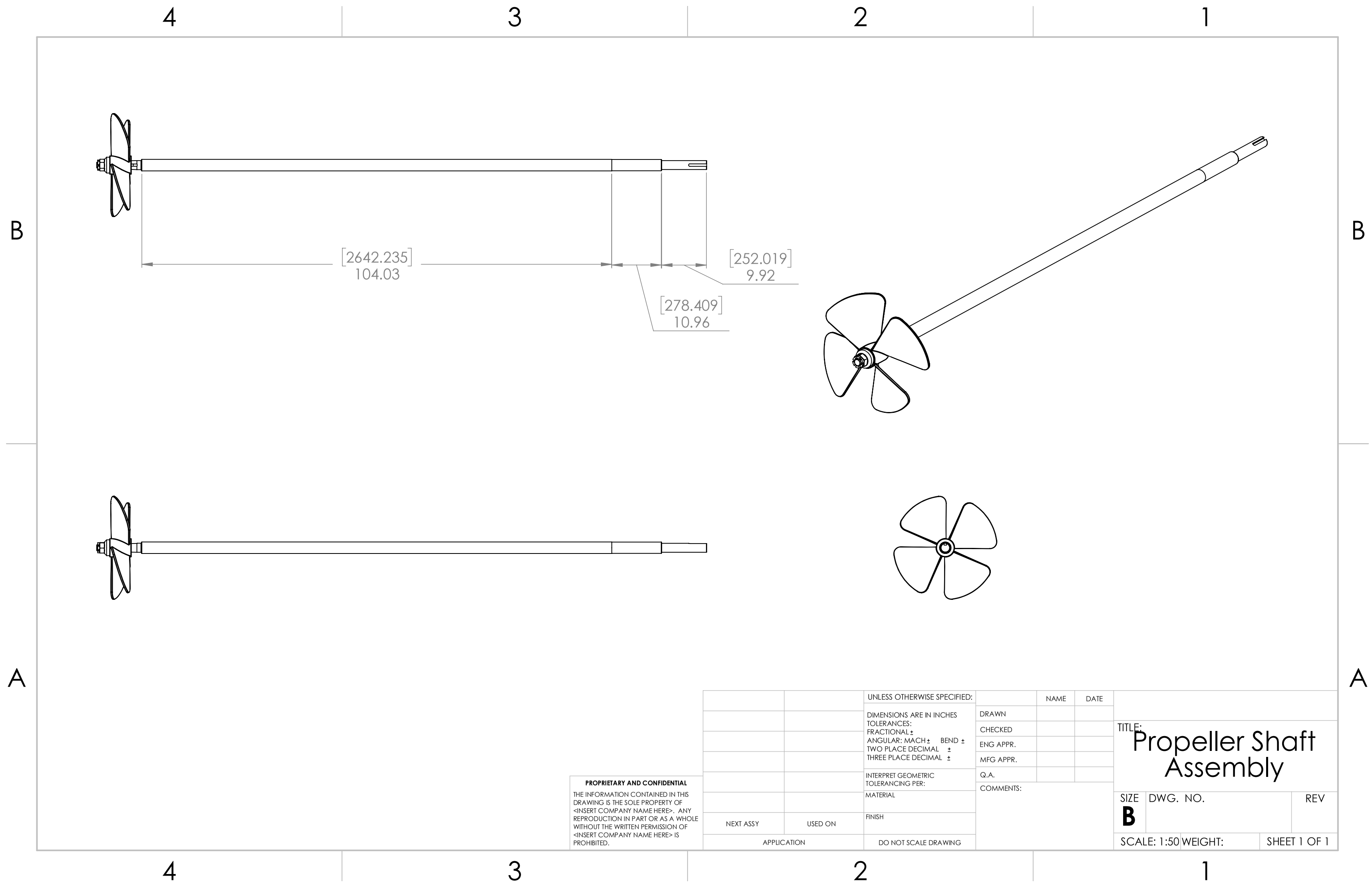

Figure B.10: Propeller shaft drawing

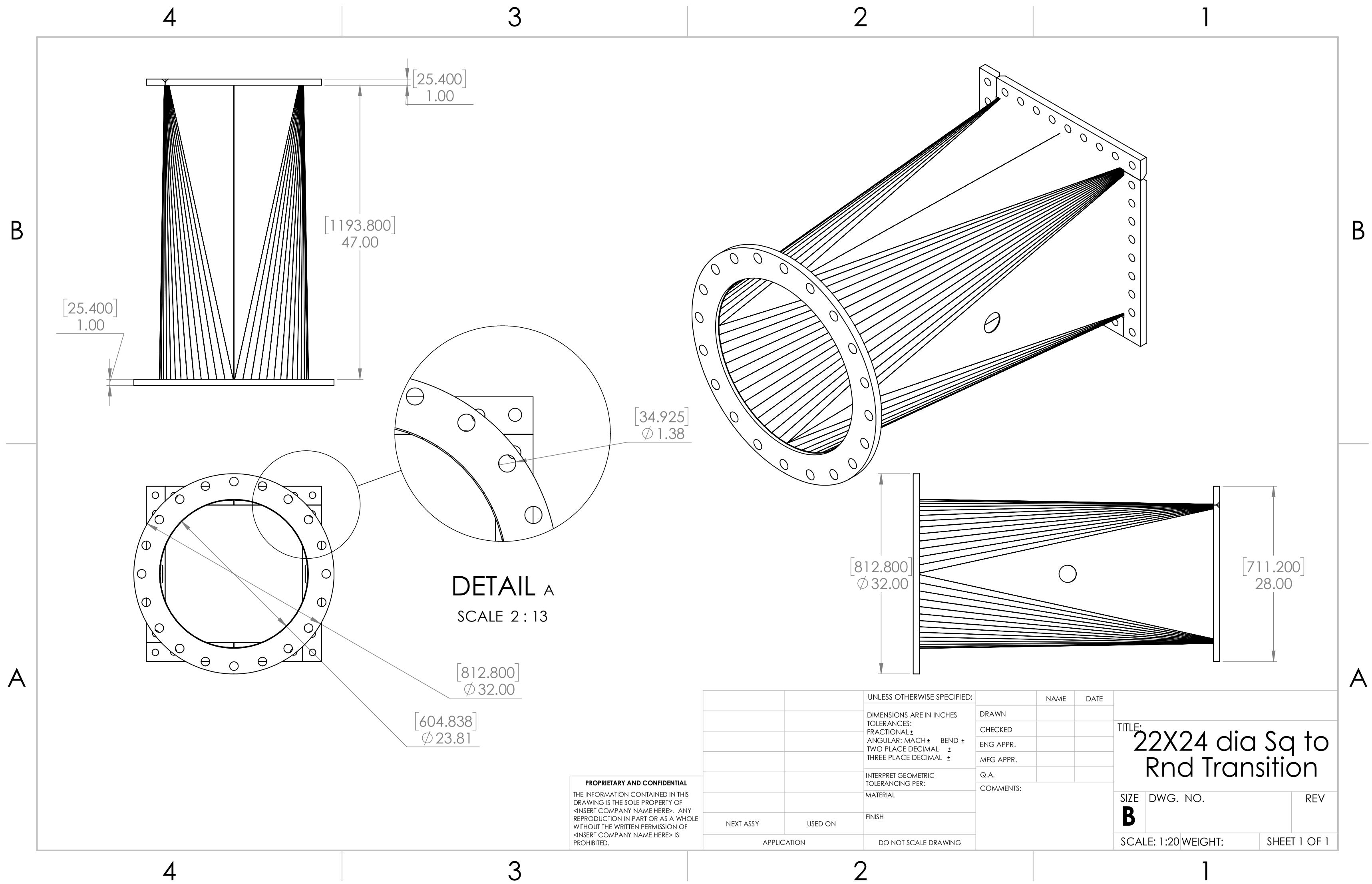

Figure B.11: Square to round transition before propeller housing

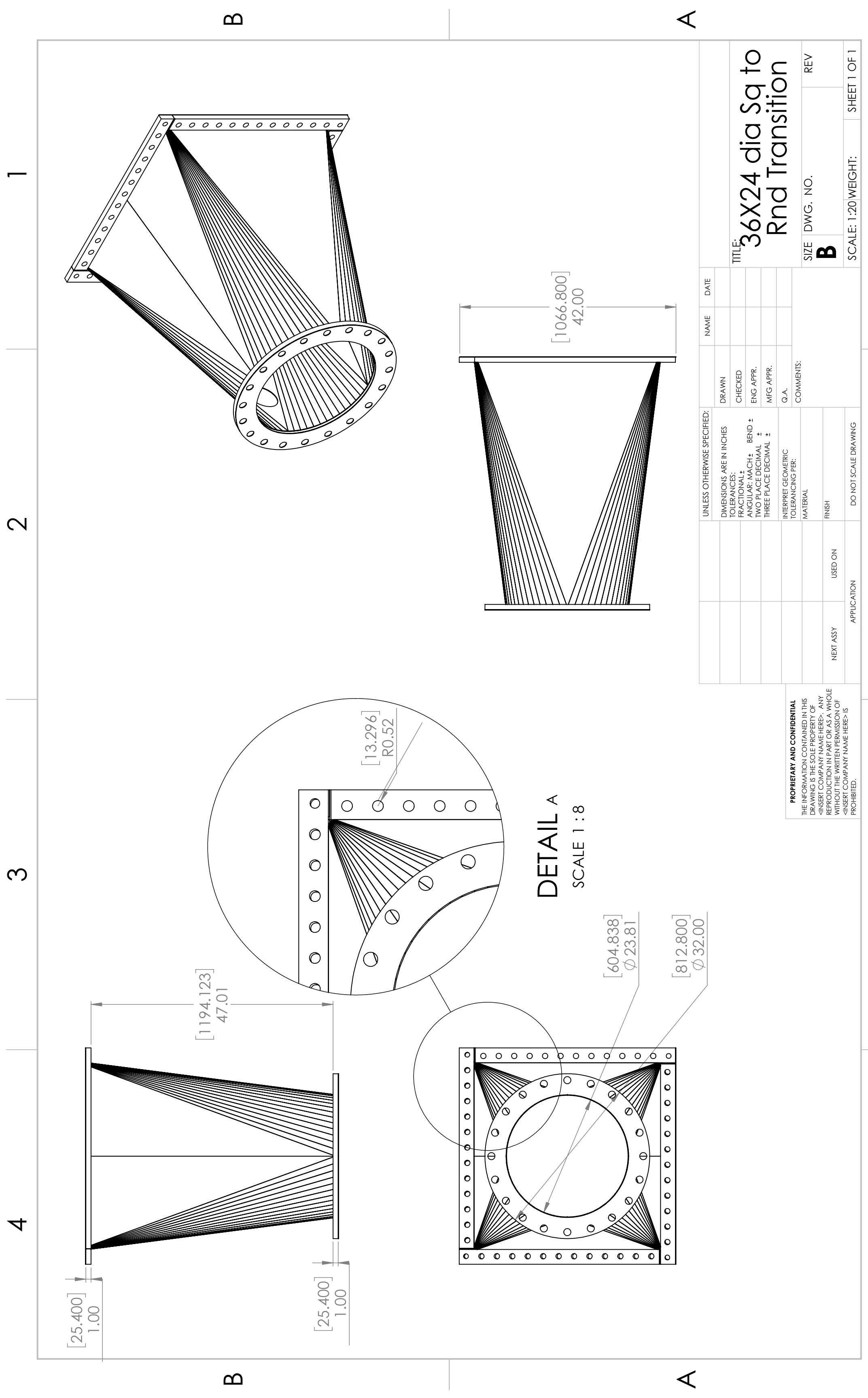

Figure B.12: Square to round transition after propeller housing